MOLECULAR INSIGHT INTO THE SLIP OF WATER AND IONS ALONG SINGLE LAYER GRAPHENE IN AQUEOUS MEDIA

BY

THOMAS GUSTAV GREENWOOD

THESIS

Submitted in partial fulfillment of the requirements
for the degree of Master of Science in Environmental Engineering in Civil Engineering
in the Graduate College of the
University of Illinois at Urbana-Champaign, 2019

Urbana, Illinois

Adviser:

Professor Rosa Maria Espinosa-Marzal

ABSTRACT

Understanding modulation of water molecule slippage along graphene surfaces is crucial for many promising applications of two-dimensional materials. Here, we examine normal and shear forces on supported single-layer graphene supported by Atomic Force Microscopy and find that the composition of the electrolyte composition affects the molecular slippage of nanometer thick films of aqueous electrolytes along the graphene surface. In the light of the shear-assisted thermally activated theory, water molecules along the graphene plane are very mobile when subjected to shear. However, upon addition of an electrolyte, the cations can make water stick to graphene, while ion-specific and concentration effects are present. Recognizing the tribological and tribochemical utility of graphene, we also evaluate the impact of this behavior on its frictional response in the presence of water. Further, this work can inspire innovation in research areas where changes of the molecular slippage through the modulation of the doping characteristics of graphene.

ACKNOWLEDGEMENTS

I would first like to express my gratitude to my adviser Dr. Rosa Maria Espinosa-Marzal for agreeing to bring me into her research group. She has given me incredible amounts of support and shown great patience while I've adjusted to and settled in this new environment, and she inspires me to be both as competent and compassionate as she has been during my time here.

Many thanks also go to Dr. SungWoo Nam and his research group, especially Dr. Michael Cai Wang and Jin Myung Kim. This work would have been much more difficult without their collaboration, and they've shown me how integral cooperation, communication, and community are to the scientific process.

Special acknowledgement goes to my personal support network of friends and family, specifically my parents. The work put into this thesis was made much easier thanks to their encouragement and reminders that they're always there for me.

Finally, I would be remiss to not thank my lab group, who made me feel so at home as the new addition: Yijue Diao, Mengwai Han, Josue Lopez, Tooba Shoaib, and the undergraduate students and other master's students who have joined in more temporary positions. Extra special thanks go to Yijue, who was my direct teacher for much of my training and has helped to set me up as a successful researcher.

TABLE OF CONTENTS

CHAPTER 1: INTRODUCTION*

With pristine graphene[1-2] being a gapless and semimetallic material, it has been found to exhibit many unique properties including ballistic electron transport,[3] large in-plane elastic modulus[4] and low coefficient of friction.[5] Graphene is seen as a potential coating material to control friction at interfaces due to its crystallinity, which allows achieving "structural superlubricity" due to the incommensurability between misaligned graphene sheets.[6-7] However, water is ubiquitous and often the origin of failure of electro-mechanical devices due to the relevance of interfacial forces like adhesion and stiction between moving components. Strategies to modulate interfacial forces will help meet future structural and functional requirements of such devices.

Intrinsically, graphene is hydrophilic with a water contact angle of ~45°,[8-9] but hydrocarbonaceous adsorbates of ambient origin may impart hydrophobicity to graphene.[8-10] The effect of water on graphene friction has been demonstrated in several works,[11-15] but the underlying mechanisms are only partially understood. For instance, density functional theory (DFT) calculations demonstrated that one monolayer of water broadens the spectral range of graphene vibrations. This effect provides new excitation channels and increases the overlap with the atomic vibrations of the substrate, both facilitating coupling and energy transfer, and thereby leading to an increase in friction.[15] The importance of liquid slippage on the viscous shear force and the friction between sliding solid surfaces has been often acknowledged.[16-18] In this context, molecular dynamics (MD) simulations[14] found that friction is higher in humid air than under vacuum. More

importantly, the authors attributed the observed friction hysteresis during loading (increase in load) and unloading (decrease in load) to the energy dissipated by the motion of the liquid molecules along the graphene surface and the pinning of water to the surface (in the absence of defects) – which resulted in a contact angle hysteresis – thereby showcasing the relevance of molecular slippage in dictating friction. Along this line, it is well-accepted that the low friction coefficient provided by graphite in humid environments stems from the water trapped between graphene sheets, which facilitates interlayer slip.[19] In contrast, ab initio simulations[20] have recently showed that water can escape from the interlayer space to react with graphene edges, emphasizing the relevance of water slippage on the lubrication mechanism and the discrepancy of results.

The discovered ultrafast water slippage in carbon nanotubes and graphene nanochannels[21-23] is a matter of scientific and technological interest but the lack of complete understanding still limits the development of graphene-based nanofluidic devices and separation membranes that enable control of flow. It is well-accepted that the slip length – defined as the ratio between the viscosity and the interfacial friction between the liquid molecules and the solid surface – is strongly related to the contact angle, which mainly stems from the effect of interaction energy between the solid and the liquid molecules on slippage.[24] To the authors' knowledge only one experimental work has reported values for the slip length of water on graphene ranging from ~0 to ~200 nm, with a most frequent value ~16 nm.[25] The large variation of the slip length was attributed to the variation of the graphene's surface charge and the interactions between graphene and the silica substrate based on MD simulations. Higher slip lengths (~60 nm) have been obtained by MD simulations in separate works.[26-27]

The focus of this work is to experimentally investigate the molecular slippage of films of nanometer thickness of water and aqueous electrolytes along graphene surfaces and its effect on

graphene friction. Monolayer graphene was synthesized via low-pressure chemical vapor deposition on 25 μm copper foils using methane as the precursor with hydrogen/argon carrier gas, as previously documented.[28] The graphene was transferred onto ~285 nm thick thermally-grown silicon oxide on silicon wafers using polycarbonate handle layers by solution etching of the copper substrate. As-prepared samples were subsequently annealed at 500ºC in a hydrogen/argon environment to improve graphene-substrate adhesion and to remove surface and interfacial polymeric residue immediately prior to measurements. Normal and lateral force measurements were conducted on graphene samples with an Atomic Force Microscope (AFM) using silicon tips in defect-free regions far away from boundaries after ensuring the absence of "pucker-up" effects.[29] Further details about the methods used can be found in the Chapter 2. The force measurements reveal an electrical double layer on graphene and ion specific effects when comparing the results in ultrapure water, KCl and NaCl solutions. We also resolve the structure of nanometer thick thin films confined between graphene and the AFM tip with subnanometer resolution through the analysis of the disjoining pressure, and interrogate the influence of the selected electrolytes on the friction force from the perspective of the stress-assisted thermally activated slip theory.[30] This evaluation provides the effect of the electrolyte composition on the molecular slippage in thin films by considering that slip is a rate process,[31-33] where the hopping of the liquid molecules from an energetically stable position to the adjacent one along the slip plane is promoted by the applied shear force at the interface, which helps overcome the required energy barrier. The results demonstrate that tuning the ionic composition of the aqueous phase is a means to modulate molecular slippage and friction.

CHAPTER 2: METHODS

Graphene Synthesis

Monolayer graphene was synthesized via low-pressure chemical vapor deposition on 25 μm copper foils using methane as the precursor with hydrogen/argon carrier gas as previously documented. The graphene samples were transferred onto ~285 nm thick thermally-grown silicon oxide on silicon wafers (Nova Electronic Materials) using poly(bisphenol A carbonate) handle layers (1.5 wt% in chloroform, MW ~45kDa) by solution etching of the copper substrate (0.1M sodium persulphate, Sigma-Aldrich). As-prepared samples were subsequently annealed at 500ºC in a hydrogen/argon environment to improve graphene-substrate adhesion and to remove surface and interfacial polymeric residue immediately prior to measurements.

Sample Preparation

Sodium chloride (NaCl) and potassium chloride (KCl) (purity>=99.0%, Sigma-Aldrich) were dissolved at room temperature in ultrapure water (18.2 MΩ-cm resistivity) to achieve concentrations of 0 mM (no salt added), 1 mM, 10 mM, 100 mM, and 1 M. The pH of the solutions was adjusted to 3.0, 6.0, and 9.0±0.2 through incremental addition of HCl and NaOH solutions. Muscovite mica substrates for reference tests were prepared by manually cleaving ruby mica of optical quality Grade #1 (S&J Trading, Inc.) just before the AFM experiments. Reference experiments were performed on the freshly cleaved mica and on a naturally oxidized silicon wafer (p-type Boron <111> 500 μm, WRS) that was cleaned with toluene, isopropanol, and ethanol, and UV-ozone treated prior to the immersion into the investigated solution.

Normal and Friction Force Measurement

A Nanowizard AFM (JPK Instruments) located in an acoustic chamber was used throughout this study. The samples were fixed in a homemade fluid-cell with 2 ml of solution. The cell was covered by a membrane to minimize evaporation of the electrolyte solutions. To exchange the solutions, a syringe was used to deplete the previous electrolyte solution in the mounted fluid-cell, which was then refilled with the next investigated solution with another syringe with extreme caution. This process was repeated three times to ensure a thorough exchange of the electrolyte solution. After 1-hour equilibration in each solution at 25ºC, normal and lateral forces were measured with AFM cantilevers (CSC38/no Al, Mikromasch) having spring constants of 0.1-0.3 N/m, as determined by the thermal calibration method.[34] The lateral sensitivities were determined in each experiment based on the method described in ref [35]. The tip used in the experiments shown here has a radius of ~34 nm, as determined by Scanning Electron Microscopy imaging. Reproducibility was confirmed by replica experiments with different tips. Prior to the force measurements, several regions were imaged in contact mode after equilibration in water for 2 hours to select relatively large areas (~5 μm x 5 μm) far away from defects and boundaries. Short tests were conducted on the selected regions to ensure the absence of "pucker-up" effects in friction loops,[36] which was interpreted as a good adhesion of the graphene to the underlying Si/SiO_2 substrate and was critical for the success of the force measurements. Each sample was divided into two halves with a diamond pen and each half was used for the measurements with DI water and with one of the salts. All friction-force measurements with the same electrolyte were conducted within the same region to ensure that the sliding direction with respect to the crystal lattice orientation was constant during each series of experiments with a particular salt. Isothermal lateral force measurements were performed as a function of load (L) and velocity (V) at each selected

concentration with a sliding length of 100 nm. The highest applied load was 20 nN, which yields a pressure of 4.3 GPa, assuming a Hertzian contact radius of 1.2 nm – calculated with elastic moduli of 155 and 1000 GPa and Poisson ratios of 0.2 and 0.17 for silicon and graphene, respectively. Force-separation curves were collected at an approach speed of 20 nm s^{-1}. The thickness of the steps and the pull-off force were obtained from the analysis of 256 curves per concentration for each electrolyte and for water. Structural changes of the graphene surface and of the tip (wear) did not occur under the conditions of our experiments. Force measurements on a single graphene sample took 10-12 hours, during which the system was observed to remain stable.

The friction-force measurements were conducted by sliding the tip along a fixed length of 100 nm (~8 traces and retraces for a single data point). Considering that the drift of our instrument is ~2 nm per 1 hr and that the slowest scan takes ~1 s (2 s for trace and retrace), the drift can be considered to have a negligible effect, and so the tip slides along the same line. The small error bars that give the friction force averaged over ~8 friction loops support that the properties of graphene do not gradually change during the sliding process.

Temperature-dependent friction-force measurements were performed using the same JPK Nanowizard AFM as the rest of the experiments, but the standard sample stage and fluid cell were replaced with the JPK PetriDishHeater/PetriDishHolder. The Si/SiO_2 substrates beneath the graphene samples were glued to 9.2 cm^2 TPP tissue culture dishes (Techno Plastic Products). Friction experiments were performed at 25° C (room temperature), 30°C, 35°C, 40°C, 45°C, and 50°C in 1 mM NaCl. The setup was allowed to thermally equilibrate for 30 minutes before each set of measurements.

The temperature setpoint to achieve the selected temperatures was determined from a calibration experiment in pure water, in which setpoint and heater temperature (measured by the JPK

PetriDishHeater) were compared to the manually measured temperature in the solution. During the calibration, the AFM was in a powered-on state but did not have a cantilever attached to the cantilever holder and was not actively scanning. The calibration was performed over the course of 60 minutes at various temperatures between room temperature and 50° C. Figure 17 demonstrates that an initial equilibration period of ~15 minutes is required to achieve constant temperature. The calibration provided the setpoint temperature required to achieve the selected temperatures in the solution, which is key to model the temperature dependent friction-force measurements using Eqs. 1-2.

CHAPTER 3: RESULTS

The Electrical Double Layer of Graphene in Aqueous Environments

The force acting between the AFM tip and graphene (see schematics in Figure 1a) was measured in ultrapure water and in NaCl and KCl aqueous solutions with concentrations ranging between 1 mM and 1 M and at an adjusted pH of 6, while approaching the tip to the surface at a constant velocity of 20 nm s^{-1}. All the measurements were conducted in the absence of any bias potential. Figures 1b-c show representative results in water and in NaCl solutions, respectively. The results for KCl can be found in Figure 6. In water, the surface force between tip and graphene is repulsive and exponentially decaying (Figure 1b, pH 6), and it becomes attractive at separations D smaller than ~4 nm. By increasing the NaCl concentration, the decay length of the exponentially decaying repulsive force decreases and agrees well with the expected Debye length of monovalent ions at concentrations ≤100 mM, which indicates that the origin for this long-range repulsion is an electrical double layer force. Moreover, control tests at 50ºC confirm that the decay length scales with $T^{1/2}$, as expected for the Debye length of an electrical double layer.[37] Detecting an electrical double layer repulsion is a key result because it indicates that graphene behaves as effectively charged in aqueous environment.

To provide more insight into the electrical double layer, the force-distance curves were modeled according to the Derjaguin-Landau-Verwey-Overbeeck (DLVO) theory at separations larger than ~3 nm, using the electrostatic potential at a plane, the outer Helmholtz plane (OHP), located a few Angstroms above the graphene surface (beyond which the ions are mobile), as one of the model parameters.[37] Details of the DLVO model can be found in Appendix A. To demonstrate that the tip is negatively charged, force measurements were also conducted on a (negatively charged) mica

surface in pure water and on a polycationic film of nanometer thickness (Figure 7). The attraction of the tip to the polycationic film and the repulsion away from the (negatively charged) mica surface reveal the negative charge of the tip under all solution conditions. Normal force measurements were also conducted on a (naturally oxidized) silicon wafer with a (naturally oxidized) silicon AFM tip to unambiguously determine the magnitude of the OHP potential of silicon dioxide surfaces, tip and substrate (Figures 8-9). With the known OHP potential of the AFM tip, the fit of the DLVO equation to the experimental results on the graphene surface provides the OHP potential of graphene (ϕ_G), as shown in Figure 1d-e; the surface charge of graphene is roughly estimated from $\sigma_G = \varepsilon\varepsilon_0\kappa\phi_G$, κ^{-1} being the Debye length, and $\varepsilon\varepsilon_0$ the permittivity of water,[37] for comparison to literature values.

The fit is very good under all conditions (lines in Figures 1 b-c and 6). The OHP potential of the tip remains negatively charged in the selected solutions (see caption of Figure 1), in agreement with reported results for silicon oxide,[38] and hence, the repulsive force in Figure 1c indicates that graphene acts as negatively charged under all conditions; see the obtained OHP potential in Figure 1d-e. The effective charge of graphene (Figure 1f) becomes more negative with gradual addition of salt and the difference in magnitude between NaCl and KCl solutions becomes more pronounced with increasing concentration, indicating that ion-specific effects become more relevant; *e.g.* the surface charge of graphene in 100 mM NaCl and KCl solutions is -0.16 nm^{-2} and -0.26 nm^{-2}, respectively.

In pure water, we find that graphene exhibits a small negative charge, σ_G~-0.008 nm^{-2}. Force measurements as a function of the pH in water support that H^+ adsorb on graphene and

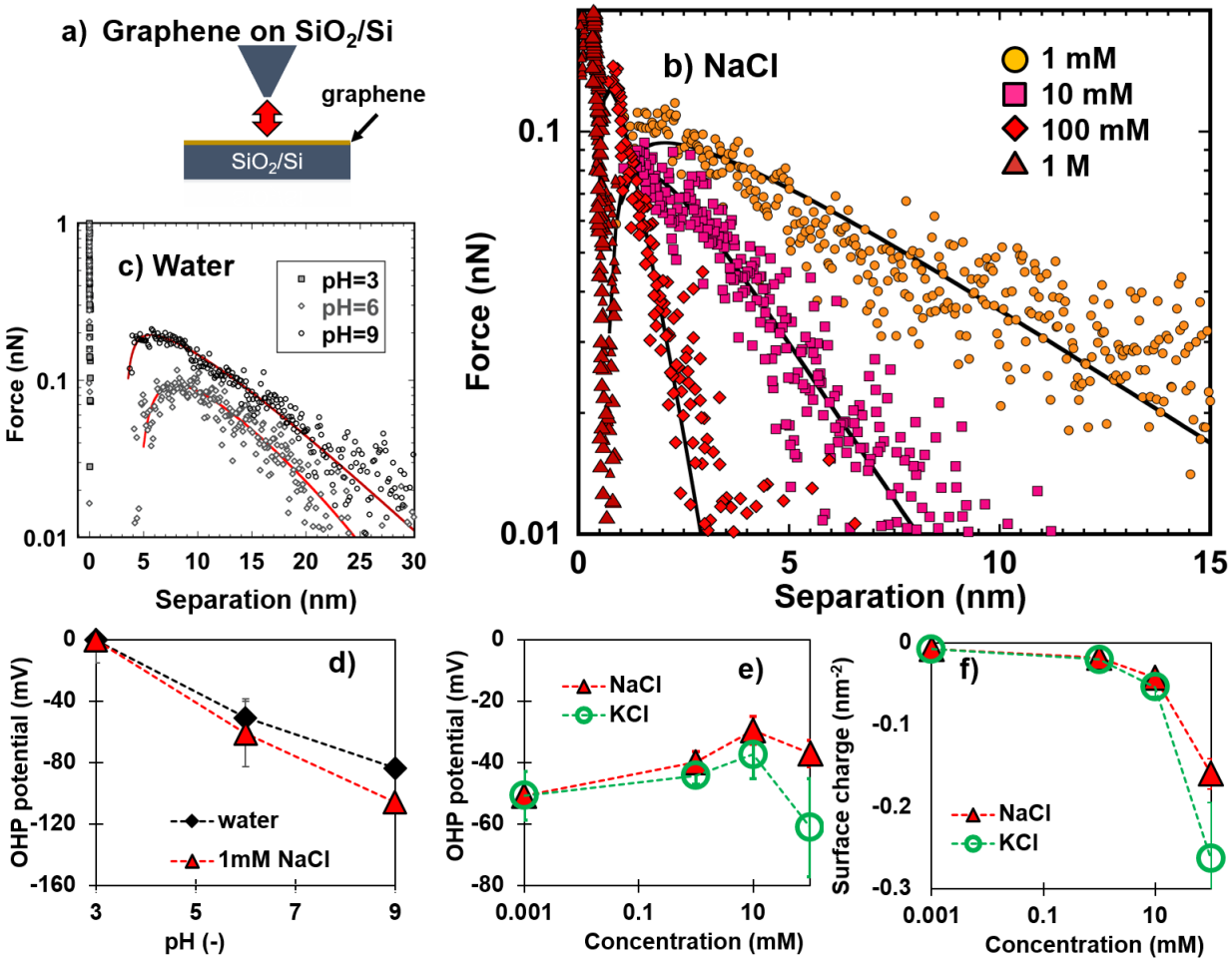

Figure 1. Surface force between graphene and the silicon tip in aqueous environment. **(a)** Schematic representation of the experimental setup where the AFM tip approaches to the graphene surface to measure normal forces. **(b)** Force between graphene and an AFM tip in DI water (different symbols represent measurements at pH 3, 6 and 9), and **(c)** in NaCl solution at the concentrations of 1 mM (circles, orange), 10 mM (squares, magenta), 100 mM (diamonds, red) and 1M (triangles, dark red). The radius of the tip is 50 nm. The surface potential of the tip obtained from control measurements (Figure 8c) is: -123(7) mV in water, -122(9) mV (1mM), -126(5) mV (10mM) and -57(13) mV (100 mM) at pH 6, and at pH 9, it is: -122(9) mV and -154(14) mV in water and in 1mM NaCl, respectively. OHP charge of graphene obtained by fitting Eq. 3 to the experimental results in **(d)** water and 1mM NaCl at different pH values and **(e)** in KCl and NaCl solutions as a function of the concentrations at pH of 6, and **(f)** calculated surface charge with the Grahame equation. The error bars show the standard deviation of fitting 8-10 force-distance curves. Although the graphene charge in water appears to be ~0 at the selected scale of the Y-axis, the value is small and negative, σ_G~-0.008(0.001) nm^{-2}. The zero separation was assumed to be the hard wall at the applied force of 5 nN (2 GPa).

counterbalance the surface charge at sufficiently high concentration (*i.e.* low pH). Figure 1b shows that at the lowest tested pH value of 3, the double layer repulsion completely vanishes, which indicates that the adsorbed ions completely compensate the surface charge. In contrast, the electrical double layer repulsion becomes stronger at pH of 9 due to the higher graphene OHP potential. The preferential adsorption of H^+ compared to Na^+ and K^+ (see binding energies in ref.[39]) can thus justify the small surface charge of graphene in ultrapure water compared to NaCl and KCl. Increasing the salt concentrations ($\leq$ 10 mM) does not lead to a remarkable change of the OHP potential, indicating that the Stern layer composition does not vary significantly for the two salts. This suggests that hydronium still outcompetes K^+ and Na^+ ions and majorly adsorbs onto graphene.

At a concentration of 100 mM, in contrast, the OHP potential abruptly decreases, especially in the case of KCl, which implies the prominent change of the Stern layer. A similar behavior has been reported for mica and attributed to the competitive adsorption of hydronium and (hydrated) metal cations to the surface.[40-42] Here, strongly hydrated metal cations remain further away from the surface surrounded by water molecules and balance the surface charge of mica less efficiently than hydronium, which causes the OHP potential to become more negative. It was observed that, because Na^+ ions are more strongly hydrated than K^+ ions, higher concentrations are needed for the Na^+ ions to replace the H^+ at the mica/solution interface.[40] It is, therefore, possible that competitive adsorption also happens on graphene and that the K^+ ions replace H^+ already in 100 mM KCl solutions, whereas a higher concentration is required in the case of NaCl, leading to the observed change in OHP potential. In fact, MD simulations have showed that K^+ ions adsorb more strongly to graphene than Na^+ at high concentrations (1 M).[43] This is also supported by the results of the interfacial structure discussed next.

Reported values of the surface charge of CVD graphene supported on Si/SiO_2 span over three orders of magnitude and are smaller than ~-0.2 nm^{-2},[25] and hence, our values are in the reported range. The origin of the negative surface charge of graphene deserves discussion. A few works have proposed the negative surface charge to arise from residue adsorption related to the sample preparation.[44] However, the reproducibility of the data across different graphene samples and the agreement of the experimental results in ultrapure water before and after the measurements in the electrolyte solutions let us exclude adventitious contamination as a source of the surface charge. First-principle DFT calculations have demonstrated that π-ion interactions lead to ion adsorption on graphene from the aqueous phase[43] and experiments corroborate that ions adsorb on graphene in contact with a liquid electrolyte.[39, 45] Cation adsorption would render positive surface charge to graphene, which would lead to an attractive double layer force, thereby contradicting our results. Anion adsorption thus appears as a potential charging mechanism,[46] with higher amount of anions adsorbing at higher chloride concentration. However, several works consider K^+ and Na^+ to adsorb more preferentially on graphene than Cl^-.[39] To test this, control force measurements at three different pH-values in water and in 1mM NaCl were carried out (see Figure 1d and Figure 10 in the SI). The results confirm that the changes in hydronium (H^+) concentration dictate the surface potential and not the chloride concentration, which let us exclude anion adsorption as the charging mechanism. While we cannot exclude the presence of a small density of oxygen functional groups on CVD graphene that could render the surface negatively charged,[25] about ~10% of the surface silanol groups of the SiO_2 substrate underneath graphene can ionize during the transfer of graphene in water at pH ~6, which could yield a maximum substrate charge of ~-0.6 nm^{-2}.[47] The largest graphene charge σ_G is ~-0.26 nm^{-2} (1 negative charge every 2 nm), and therefore, the charge of the

underlying silica oxide substrate combined with partial screening by the graphene[48-49] could be responsible for the charge of the graphene surface, as well.

Interfacial Nanostructure

When the AFM tip is slowly approached to the surface, ions and water are squeezed out and the remaining molecules rearrange in the films confined by the solid surfaces. When the distance (D) between tip and graphene becomes smaller than ~3 nm, a stronger repulsion with superposed steps is measured (see arrows in Figure 2 for NaCl and Figure 11 for KCl). This short-range repulsion between the confining walls (also called disjoining force or pressure) is originated not only by dispersion and electrostatic interactions but it is also affected by the adsorption of the molecules to the surfaces and by structural (or layering) effects of the thin films of nanometer thickness.[50] On atomically flat surfaces, like graphene, the liquid molecules tend to arrange in layers. When the tip approaches the surface, it jumps from one to the next layer,[51] which appears as a step in the force-separation curve. This means that layers of water and ions located close to the graphene surface are probed by the tip.

The size of the steps gives roughly the thickness of the interfacial layers of ions and water. The inset in Figure 2a displays a bubble diagram of the step size measured in water (black) and in the NaCl (red) and KCl (green) solutions, where the bubble size gives the relative frequency of the steps of this size. In water, the thickness of the steps is of the size of the water molecule, ~2.7(0.3) Å. The presence of Na^+ ions is reflected in an increase of the step size from ~2.7(0.3) to ~ 4.5 Å (yellow region) and 7.4 Å (blue region) in 1mM NaCl solution, which indicates that ions (with their hydration shells) populate the interfacial region, along with water, as also observed in SFA experiments with mica elsewhere.[40, 52] The small size of the steps displaced at the highest forces

(~3.1 Å, grey region) suggests that water is still present at the graphene/NaCl solution interface. Increasing the NaCl concentration leads to a progressive decrease in the step size, indicating that layers with less hydrated ions are probed with the tip at higher concentrations, but water is always present close to the graphene surface and removed at the highest applied pressures (see the red bubbles in the grey region). The structure of the thin films felt by the tip in KCl is different. The smaller size of the steps (3-4 Å, yellow region) indicates that the tip probes layers rich in ions but less hydrated than in the case of Na^+ as inferred from their smaller size. Further, the absence of steps in the range 2-3 Å (grey region) suggest that K^+ ions has displaced interfacial water layers, so that they interact more directly with the graphene surface. Note that Na^+ is a strongly hydrated cation with multiple near-surface hydration states, while K^+ has a lower hydration strength.[53] Thus, the measured interfacial structure is consistent with MD simulations of the graphene/electrolyte interface, which show that ions with high hydration strength (*e.g.* Na^+) might not penetrate through the interfacial water layers, while larger ions (*e.g.* Rb^+ or K^+) can dehydrate and interact more closely with graphene.[54]

At pressures above 1 GPa, no more layers are resolved, and therefore, the composition of the thin films cannot be further examined. Due to the uncertainty about the location of the absolute separation in AFM experiments, the true thickness of the confined liquid film cannot be precisely determined. Nevertheless, previous experiments[12] and MD simulations[14] showed that a pressure higher than ~13 and 30 GPa, respectively, needs to be applied to squeeze-out the water trapped between a tip and graphene, independently of the assumed hydrophilicity of the graphene surface. This range of pressures is ~4-10 times larger than the maximum value applied in our experiments to prevent the damage of the tip. Although the composition of this thin film cannot be examined

by squeezing out layers, its impact on adhesion and on the shear force can be investigated by measuring the pull-off force and the friction force, respectively.

Figures 2b and 2c summarize the pull-off force that is measured when the tip is retracted from the surface. The addition of 1mM KCl and NaCl decreases the pull-off force to the half (~1.5(0.5) nN in water). A change in the pull-off force is observed in KCl solutions, first decreasing and then increasing at concentrations ≥ 100 mM, while this increase happens at ≥ 1 M in the case of NaCl and is much less prominent. This different behavior reflects the effect of the different composition of the confined fluid film on adhesion. The pull-off force is reduced with respect to its value in air (~5 nN),[5] due to reduced van der Waals (dispersion) forces (see Hamaker constant in Appendix A).

In theory, the adhesion energy between two solid surfaces in an electrolyte solution has dispersive, structural and electrostatic contributions.[37] Obviously, the distance between the surfaces increases when the thickness of the confined liquid film is greater, which decreases the dispersive contribution (van der Waals) to the adhesion energy. The layered structure of the fluid film leads to multiple adhesive minima that are less strongly adhesive than the adhesion between the solid surfaces. This may justify the decrease in the pull-off force in the electrolyte solutions (with more layers) compared to ultrapure water, as reported for other systems.[37] At high concentrations, the electrostatic contribution originating from ion-ion correlations becomes more significant.[55] Here, an excess of counterions on one side is correlated with a lack of counterions on the opposite side, causing an overall attraction, and an increase in adhesion energy. It is thus possible that ion-ion correlations become significant for KCl at concentrations above 10 mM, when the pull off force is seen to increase, while in the case of NaCl, they become relevant only at concentrations ~1 M. This different behavior of the two electrolytes is supported by the higher

amount of interfacial water in the NaCl thin films that was inferred from the size of the layers (inset in Figure 2b). Note that a similar trend was observed for $NaNO_3$ and KNO_3 when confined between mica surfaces,[40, 52] and hence, this behavior is not unique to graphene.

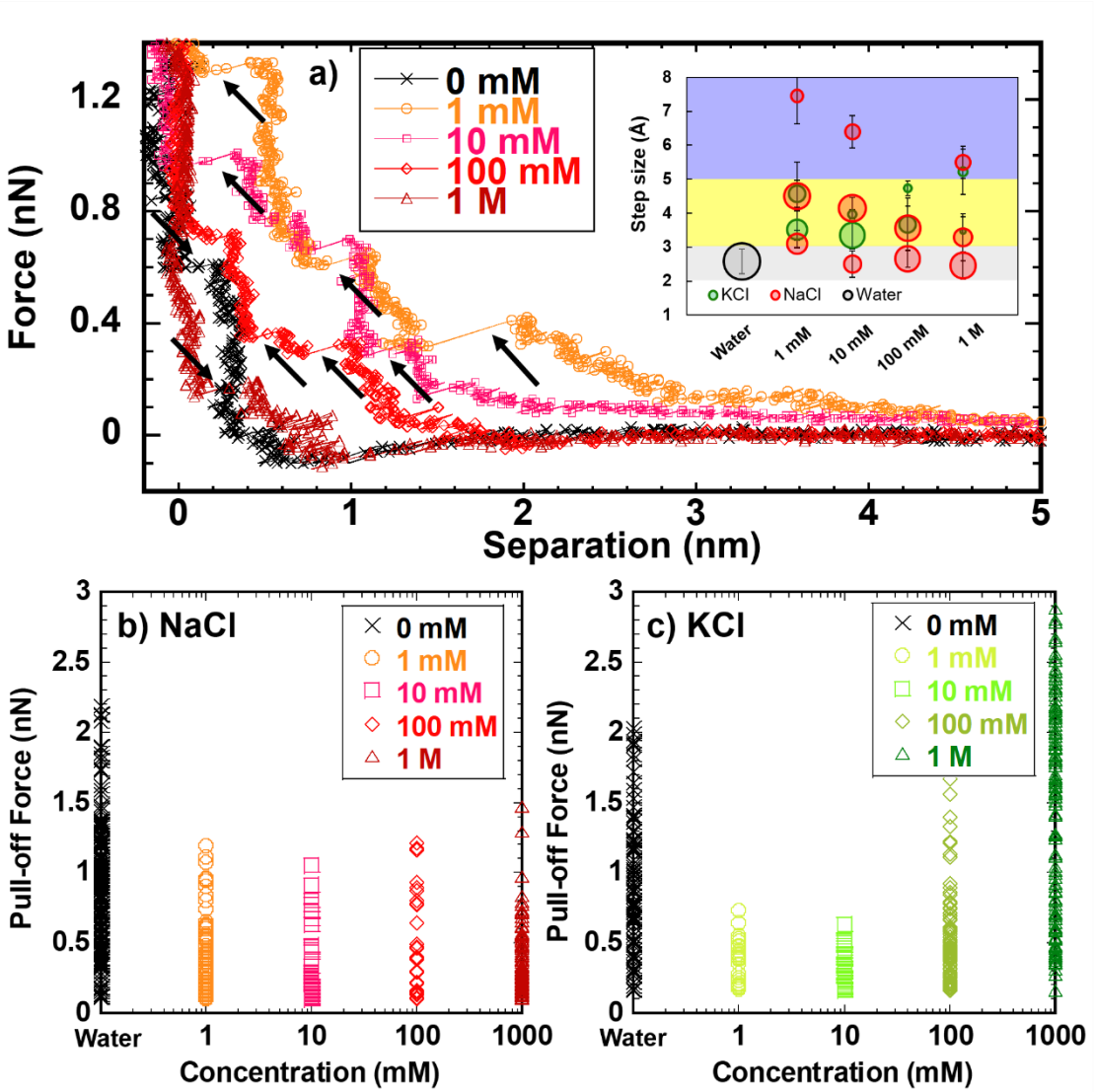

Figure 2. Structure of the graphene-electrolyte interface. **(a)** Short-range surface force as a function of the separation between the silicon tip and graphene in water (0 mM) and NaCl solutions. The inset shows a bubble diagram of the step size in NaCl (red) and KCl (green) solutions as a function of the concentration and in water (black). The size of the bubble is proportional to the frequency of the steps with this size. Three regions are distinguished with shades: 2-3 Å (grey), 3-5 Å (yellow) and 5-8 Å (blue). **(b-c)** Pull-off force as a function of the concentration in b) NaCl and c) KCl solutions. Radius of the tip is 50 nm.

Friction Between a Silicon Tip and Graphene in Aqueous Environments

Friction was first measured as a function of normal load at constant sliding velocity of 0.2 μm s^{-1} (Figure 3) by increasing the applied normal load stepwise (loading curve, empty circles) and then decreasing (unloading curve, filled diamonds). Friction increases first in a linear fashion until an abrupt increase is observed at ~60 nN (Hertzian stress~10 GPa). While this sudden increase in friction could indicate the onset of wear, the low friction was recovered in the unloading curve, thereby demonstrating the reversibility of the mechanism of energy dissipation, and the absence of damage. This is also consistent with friction measurements on CVD graphene by others, which showed that much higher contact stresses and a much higher number of cycles are needed to damage CVD graphene.[56] Based on previous MD simulations,[12, 14] it is possible that the squeeze-out of hydration layers could be related to the abrupt increase in friction at ~60 nN in Figure 3. Therefore, in the velocity-dependent friction-force measurements discussed next the load was maintained smaller than 20 nN (~5 GPa) to avoid this transition from happening.

Figure 4 shows representative results of the friction force, F_L, between graphene and the tip as a function of the sliding velocity, V, and at loads ranging from 0.5 to 20 nN in water and in NaCl and KCl solutions at the selected concentrations. It is evident that friction increases with both load and velocity under all investigated conditions. Further, friction decreases with addition of salt down to a minimum at a concentration of 100 mM, and it increases in 1 M solutions, especially in the case of NaCl. The electrolyte concentration has an intricate effect on the slope and intercepts of the friction *vs.* velocity curves, which will be analyzed later. The reference measurements on the underlying Si/SiO_2 substrate in aqueous solutions feature (i) much higher friction compared to graphene and (ii) a pronounced decrease in friction with velocity throughout the whole range of

investigated sliding velocities (Figure 12), which indicates that the mechanism of frictional dissipation in Figure 4 is greatly determined by the graphene surface.

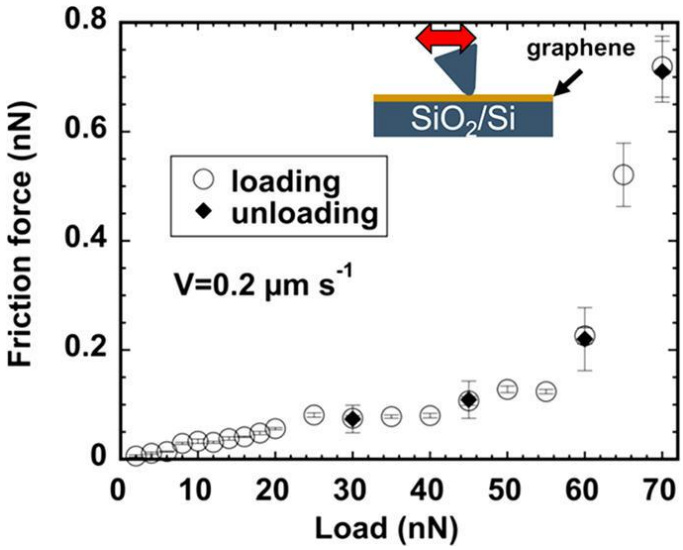

Figure 3. Friction force between graphene and the silicon AFM tip in an aqueous environment. **(a)** Schematic representation of the friction force measurements with the tip sliding laterally near the graphene surface. **(b)** Friction force between graphene and the silicon tip as a function of load at constant sliding velocity of 0.2 μm s^{-1} measured while the load is gradually increased (loading, empty circles) and decreased (unloading, filled diamonds). Tip radius is 34 nm. The inset shows a schematic representation of the friction force measurements with the tip sliding laterally near the graphene surface.

Shear-Assisted Thermally Activated Slip Theory

The friction-force measurements are evaluated in the light of the shear-assisted thermally activated slip theory.[57] We treat the molecular slip along the slip plane as a rate process in the context of Eyring's theory,[31-32] in which a shear force applied on the molecule couples with its thermal energy to increase the rate of flow or slip.[30] For slip to occur, the molecule, initially in an equilibrium position (an energy minimum), needs to pass over an energy barrier E_a (the transition

state) before reaching the adjacent energetic minimum. The applied shear force on the molecule has the effect of lowering this energy barrier by $F_{\mathrm{L}}\lambda$, which increases the slip rate. λ is the shear-activation length and represents the displacement of the molecules from the energetic minimum to the transition state,[57] as shown in Figure 5a. Considering that the slip rate of the water molecules, ν, is increased by the applied shear force according to $\nu \sim \nu^{*}\exp(-(E_a - F_{\mathrm{L}}\lambda)/k_{\mathrm{B}}T)$, k_{B} being the Boltzmann constant, T the absolute temperature and ν^{*} the vibration frequency in a reference state, the following expression is obtained for the shear force F_{L}:[58]

$$F_L = \frac{E_a}{\lambda} + \frac{k_{\mathrm{B}}T}{\lambda}\ln(V/V_0)$$

Eq. (1)

$V = d \cdot \nu$ being the sliding velocity, d the hopping distance of the molecules and $V_0 = d \cdot \nu^{*}$ a reference velocity.

Many experimental and computational studies have showed that the shear stress between two surfaces with a lubricant film scales with the logarithm of the sliding velocities; see recent review.[30] In some of these works, the influence of the pressure (P) was additionally considered. For instance, Evans and Briscoe[68] considered the effect an increase in the energy barrier,[33, 59] *i.e.* $E_a + P \cdot \Omega$, where Ω is the so-called pressure-activation volume. Since both the contact area and the distribution of forces among the confined molecules are unknown, we refrain from describing the slip rate process in terms of pressure and activation volumes, and instead, we consider the increase of the energy barrier as $E_a + L \cdot \gamma$, where L is the load and γ a pressure-activation length; this approach was followed in a recent AFM study of the oxidation of graphene driven by the tip force.[60] Here, $L \cdot \gamma$ represents the work applied to move the molecules vertically away from the

surface a distance γ against the applied pressure (like a dilation), which is required for slip to happen. This leads to a modified model for the shear force:

$$F_L = \frac{E_a + L \cdot \gamma}{\lambda} + \frac{k_B T}{\lambda} \ln(V/V_0)$$

Eq. (2)

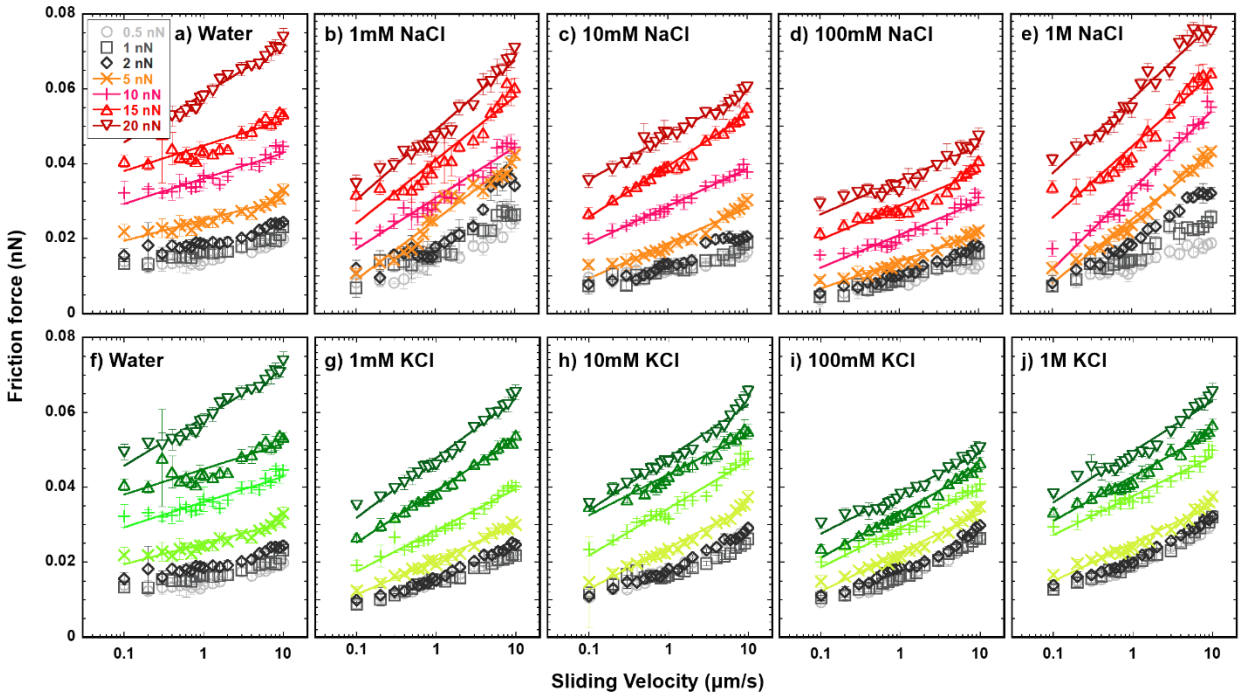

Figure 4. Friction force between graphene and the AFM tip as a function of velocity and normal load. Measurements were taken in NaCl (a-e, shades of red) and KCl (f-j, shades of green) solutions at the concentrations of **(a, f)** 0 mM (water), **(b, g)** 1 mM, **(c, h)** 10 mM, **(d, i)** 100 mM, and **(e, j)** 1 M, at a pH of 6.0±0.2. Error bars give the variation in friction across eight friction loops. Light grey, grey, and black represent applied loads of 0.5, 1, and 2 nN respectively, while the colored shade from light to dark (in red for NaCl and in green for KCl) indicates applied loads from 5 to 20 nN (see legend in a). According to Hertzian contact mechanics, the average stress ranges from 1.3 to 4.3 GPa for loads between 0.5 nN and 20 nN, given a tip radius of 34 nm. A magnification of the results at loads from 0.2 nN to 2 nN is shown in Figure 13. The solid lines show the fits of Eq. 1-2 to the experimental results.

The linear relation between energy barrier and the normal load assumes that the structure and compliance of the molecules does not change during the sliding process. Although more complex models to describe the change of the energy barrier with load are possible,[30] a linear relation leads to regression coefficients better than 0.95 here, and hence, it is sufficient. Eq. 2 thus accounts for the effects of pressure and shear stress on the molecular slip of a fluid film of a few nanometers in thickness, with slip rate: $v \sim v^* \exp(-(E_a + L \cdot \gamma - F_L \lambda)/k_B T)$. Note that the parameters λ and γ are defined for the total applied normal load and shear force in the confined liquid films, respectively, and not for the force applied on a single molecule, as in Eyring's original model.

The logarithmic dependence of the measured friction force with the sliding velocity in Figure 4 is consistent with Eqs. 1-2, and the lines represent the fits to this model. At a specific load, the slope of each F_L *vs.* V curve gives λ, while $\Sigma = E_a + L \cdot \gamma - k_B T \cdot \ln(V_0)$ is obtained from the intercept. The slope of Σ *vs.* L gives γ and the intercept provides $E_a - k_B T \cdot \ln(V_0)$. In order to unambiguously determine E_a, it is necessary to determine the reference velocity V_0, for which we have performed separate temperature-dependent friction-force measurements. Figure 14 shows that the friction force (at constant velocity of 1 μm/s) decreases linearly with increasing temperature for each specific load, as expected for a thermally activated process and from Eq. 2. Figure 15 confirms this trend for another series of experiments as a function of the sliding velocity, load and temperature. It is noted that the range of accessible temperatures in our AFM is very narrow (25-50ºC), which hinders a precise determination of V_0, but the average value of 40 m/s is reasonable considering the residence time of water molecules in bulk solution and in the hydration shell of ions (~10^{-11} s [61]); see SI for detailed information about V_0.

Shear Activation Length and Thermal Activation Energy

The obtained fitting parameters (λ, γ and E_a) are summarized in Figure 5. It is evident that λ decreases significantly with increasing normal load from ~2.5 to 1 nm (Figure 5d-e), which likely results from the increase in the area by ~4.5 with the increase in load from ~2 to 20 nN.[60] Reference tests on mica give λ values ranging from ~0.9 to 0.2 nm for water (Figure 16), and therefore, much smaller than for graphene, meaning that, under shear, water sticks to mica more than to graphene. This is consistent with the greater slip length of water on graphene compared to mica.[62] The addition of 1mM NaCl and KCl causes an abrupt decrease in the shear-activation length (Figures 5d and 5e), *i.e.* the molecules slip less easily than in pure water. Note that Figure 6b only shows results at loads ≥ 2 nN in NaCl solutions, because a power law often describes these results better than a logarithmic function (Figure 13).

The change of λ is ion- and concentration-specific. The change of the shear-activation length with NaCl concentration is intricate: there is an initial decrease when 1mM NaCl is added to the solution (similar to 1mM KCl), but further increase in concentration leads to an elongation of the activation length, and a concentration of 1M NaCl causes λ to significantly contract again, indicating that there are several competing mechanisms at play. In contrast, the shear-activation length in KCl is less dependent on concentration. This electrolyte-specific response of λ may be related to the different composition of the confined fluid films. The layer-size distribution in NaCl solutions suggested the presence of interfacial water and of Na^+ with multiple hydration states, while less water and less hydrated ions were present in the KCl films (inset in Figure 2). We thus speculate that the variation of the shear-activation length reflects the different hydration states of the cations, with higher values associated to greater amounts of water in the fluid film. With an increase in NaCl concentration, more Na^+ ions increasingly populate the fluid film; these ions are

more strongly hydrated, which leads to an increase in the amount of confined water in the thin films. The dramatic decrease in λ in 1M NaCl coincides with the increase in adhesion and in the presence of layers with less hydrated Na^+ ions, as described earlier.

The ions significantly reduce the thermal activation energy from ~26 k_BT to ~20 k_BT and ~21 k_BT in KCl and NaCl solutions, respectively (Figure 5b). Based on Eyring's slip theory, the thermal activation energy for slip arises from the distortion of the interactions with the molecules in neighboring layers, *i.e.* here, the hydrogen bond network between the interfacial water layers and the interaction strength between the water molecules and the surface. The presence of the ions is known to disturb the hydrogen bond network of the interfacial water,[63] which justifies that the molecular slip requires lesser thermal activation energy in the electrolyte solutions than in pure water. Ion-specific effects are reflected in the pressure-activation length of the confined films: note that γ increases with NaCl concentration and it abruptly decreases in 1M NaCl, while it remains approximately constant in KCl. The higher dilation seen at intermediate NaCl concentrations might be also associated to the higher amounts of retained water by the confined Na^+ ions in the thin films, but more studies are needed to understand these results.

Comparisons to literature are limited to surfactant monolayers and polymers confined by different solid surfaces. For example, reported values for Langmuir-Blodgett monolayers on mica are:[59] E_a~26 k_BT and shear-activation volume (instead of "length", λ) ~3.3 – 5 nm^3, *i.e.* larger than the molecular volume of the surfactant ~0.5 nm^3, which was interpreted as a cooperative or collective motion of 5-10 molecules. We have obtained a very similar thermal activation energy and a smaller shear-activation volume of ~$\lambda \cdot A_{mol}$~0.11 nm^3 for λ=2 nm in pure water (A_{mol}=area of water molecule), perhaps due to the smaller size of the molecules in this work. While the two systems

are chemically different, and hence, a quantitative comparison is not targeted here, the results are of the same order of magnitude.

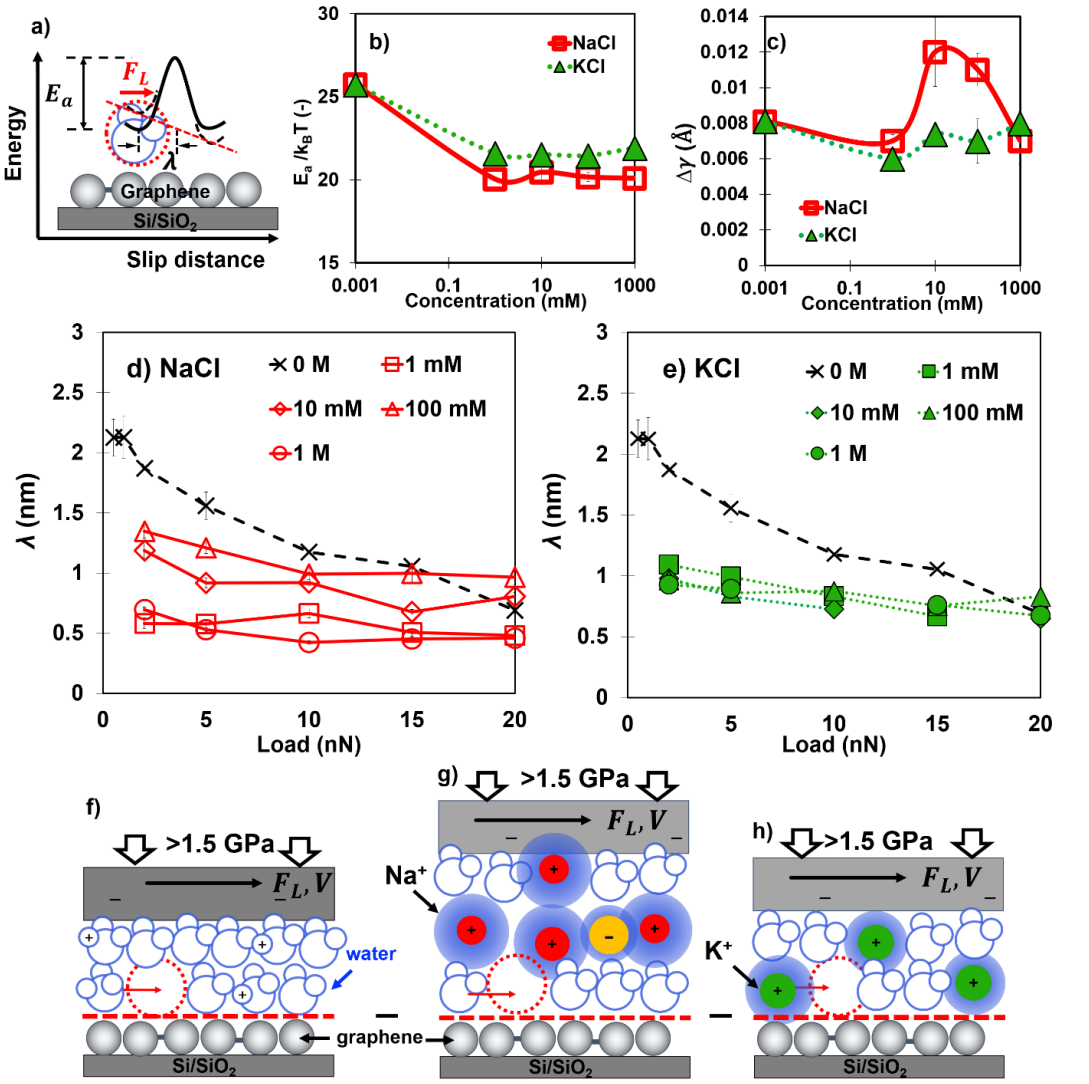

Figure 5. (a) Illustration of the shear-assisted thermally activated slip in films of aqueous solutions confined between an AFM tip and the graphene surface. **(b)** Thermal activation energy (E_a/k_BT), **(c)** displacement along the normal direction ($\Delta\gamma$), and **(d-e)** shear-activation length (λ) in water, **(d)** NaCl and **(e)** KCl solutions. The error bars show the root-mean-square errors of the fits and they are often smaller than the symbol size, and, therefore, not always visible. The cartoons show the molecular slip **(f)** in water and in 10 mM **(g)** NaCl and **(h)** KCl solutions. In 10 mM NaCl, the Na^+ ions retain larger amounts of water than in KCl at the same concentration. The graphene is represented by the grey carbon atoms above the Si/SiO_2 substrate. The red dashed line shows the proposed location of the slip plane. In the electrolyte solutions, the observed change in λ could also imply a change of the slip plane location, but the low surface charge supports that the electrostatic attraction of ions to the surface is weak, and therefore, we speculate that it is still located at the graphene surface.

CHAPTER 4: DISCUSSION

Several works have reported electrolyte-specific graphene properties, which are consistent with an ion-specific composition of the graphene/solution interface. For instance, the conductance of graphene in liquid-gated transistors is strongly affected by changes in ionic strength, pH and the type of ions present, which has been proposed to rely on changes of the electrical double layer.[44] This work has scrutinized the electrical double layer on graphene supported on Si/SiO_2 substrate for two electrolytes at various concentrations and pH values. As inferred from the OHP potential, distinct Stern layers form on the graphene surface as a function of the electrolyte composition, which is attributed to the different adsorption strengths of hydronium, potassium and sodium ions. Applying high pressures ($\gtrsim$0.5 GPa) with an AFM tip against the graphene surface enables the confinement of an aqueous film of nanometer thickness ($<$3 nm) that is composed of layers of water molecules as well as ions, which maintain the electroneutrality of the system. The normal force measurements allowed us to partially resolve the structure of these thin films with subnanometer resolution. The prominent difference between the structure of the confined aqueous films is proposed to rely on the higher hydration strength of the Na^+ ions, which remain further away from the surface and retain more water in their hydration shells compared to K^+.

The friction between the AFM tip and graphene was evaluated in the light of the shear-assisted thermally activated slip theory, which provided insight into the molecular slippage. In the case of pure water, Figure 5f shows two layers of water molecules but there might be more, along with a small concentration of hydronium to maintain electroneutrality; here, it was assumed that the surface charges are ~ 2 nm apart (~-0.3 nm^{-2}). While the upper wall moves laterally at constant velocity, the water molecules and some hydronium slip along the graphene plane. A large shear-

activation length λ implies that the molecules are not pinned to the surface under shear, thereby also leading to a large slip length. The ease of the water molecules to slip is reflected in the large shear-activation length on graphene compared to mica (Figure 16), consistent with the greater slip length of water on graphene.[18, 62]

As deduced from the significant decrease in λ with addition of only 1mM salt, it appears that a small amount of Na^+ and K^+ ions is sufficient to "stick" water to the graphene. Figures 5g and 5h illustrate two aqueous films at intermediate concentrations, when slippage is favored in NaCl solution compared to KCl. The sensitivity of slippage to the electrolyte composition implies that both cations and anions must populate the films; note that the concentration of cations cannot be increased without including sufficient anions in order to maintain electroneutrality. The observed ion-specific effects on the slippage are consistent with the hydration strength of the cations: strongly hydrated Na^+ ions retain more water in the confined films and do not penetrate the hydration layers, which promotes slippage. Note that higher amounts of trapped Na+ ions (and anions) at higher NaCl concentrations should retain more water, which would be consistent with the observed increase in shear-activation length. This does not happen in the case of K+, a weaker hydrated cation. These results corroborate previously observed phenomena of varying mobility of hydrated ions in confined configurations such as through carbon nanotubes and induced swelling of multilayer graphene and graphene oxide membranes.[64-65] Furthermore, these findings indicate that tuning the ionic solution composition can be a strategy to modulate the molecular slippage in graphene nanochannels.

The implications of this work for the tribological performance of graphene in an aqueous environment are discussed next. Here, the origin of friction is the irreversible work dissipated ($F_L \cdot \lambda$) when the molecules fall from the transition state to the adjacent energetic minimum. It appears

that the addition of an electrolyte to pure water causes a reduction of the thermal activation energy and of the shear-activation length at several concentrations, both results *conversely* affecting the friction force; note that the overall change in friction in Figure 4 appears to be small, so that, interestingly, both changes partially compensate each other. The lowest friction is attained at a concentration of 100 mM in both salts, which indicates that, here, the effect of the ions on lowering the thermal activation energy dominates over the slippage along the graphene surface. One intriguing result is that at the highest NaCl concentration (1M), the "sticking" effect to the graphene seems to take over, as shown by the higher increase in friction compared to KCl at the same concentration. This, however, cannot be rationalized based on our simple model. It is possible that atomic-scale roughness introduced *via* the confinement of ions contributes to this result. However, proving this hypothesis requires consideration of other theories and models that are out of the scope of this work. Finally, while the structural superlubricity of graphene may be impaired by the presence of water, as proved in theory,[15] our results suggest that a proper selection of electrolyte may be used to tune the lubricious properties of graphene when water is present in the system.

CHAPTER 5: CONCLUSIONS AND FUTURE WORK

Summary of Current Findings

This study demonstrates that modulating the electrolyte composition may be a means to control the molecular slip, and thus, fluid flow through graphene nanochannels, as well as friction at graphene contacts in an aqueous environment. Graphene interacts with molecules and ions in its close vicinity via the delocalized π-electrons, and hence, molecular adsorption is sensitive to graphene doping.[66-67] Given the relevance of the adsorption strength of the liquid molecules to the surface on the considered slip-rate process, the present study opens a new avenue of research about how modulating the electronic properties of graphene could be used to tune the interfacial motion of fluids, the flow in graphene nanochannels, and friction in the presence of a lubricant film. While we will examine the effects of substrate-induced doping of graphene on molecular slippage and friction in the near future, the effects of the pH and temperature on these phenomena still remain open questions that also need to be addressed. Further, we have shown that the measurement of normal and lateral forces can provide a conceptual understanding of the graphene-electrolyte interface. This type of study can also be extended to probe the influence of adsorbed/intercalated ions on/underneath graphene on the transport properties of solution-gated graphene FETs and on interfacial properties of semiconducting 2D transition metal dichalcogenides. Characterization of 2D supercapacitor electrode surfaces via this approach may also enable identification (at the subnanometer level) of the relative contributions of ion adsorption versus Faradic mechanisms, for both aqueous and non-aqueous electrolytes, including ionic liquids.

Outlook and Future Investigations

The results of this work indicate many intriguing lines of research related to both the fundamental properties of graphene in aqueous environments and potential applications for graphene as an emerging material. Some applications are mentioned in the previous section, such as in transistors, as a low-friction coating, and as the material for nanochannel construction, and further insight into the molecular interactions of graphene with water and water-based solutions will benefit all such applications in some way.

An additional area these results prompt interest in is graphene as a method of filtration membrane functionalization. Due to challenges in synthesis, early investigations into graphene as a membrane material began as molecular dynamics simulations. They indicated that nanoporous monolayer graphene held the potential to be a dramatic improvement over current membrane materials.[21] Since then, many studies both simulated and experimental have continually demonstrated the promise of graphene.[68] However, despite the massive interest in graphene membranes and an increasing number of approaches to produce usable graphene membrane technologies there is still a lack of knowledge regarding many of the fundamental properties of graphene in aqueous conditions relevant to water treatment and desalination. These fundamental properties influence many of the factors, such as interfacial fluid viscosity and hydrodynamics,[18] related to membrane performance parameters like water flux. There is recent evidence that many of these fundamental properties can be modulated, primarily through doping of graphene, by adjusting factors like solution composition and substrate,[69] and this work continues to provide evidence of graphene's promise. Its apparently high intrinsic molecular mobility and tunable surface properties suggest that graphene has the potential to contribute to advanced, more functional, and more efficient filtration performance.

There are three immediate avenues to explore following the results of this research to better examine and understand graphene's potential in aqueous environments. The first is to quantify the hydrodynamic slip length mentioned earlier in this work. The shear-activation length investigated here demonstrates the mobility of molecules near surfaces, but the slip length provides a more direct link between the hydrodynamic properties of the fluid and the surface. The second is to observe differences between graphene in differently doped states. This work only used Si/SiO_2 as a substrate, but we expect modifying the substrate with polyelectrolyte coatings as in ref.[69] or metals will change graphene's surface properties and therefore its interactions with aqueous media. Finally, new experimental methods can provide new or more accurate information. While the AFM is a versatile tool, it is limited in detailed descriptions of surface properties due to dissimilar surfaces and an ambiguous tip to surface distance. The surface forces apparatus (SFA) can use similar surfaces and measures much more accurate distances between surfaces, providing benefits like the simulation of nanopores found in nanofiltration membranes and results suitable for more in-depth analysis of force-distance curves. Generally the surfaces used in an SFA are mica, but there is demonstrated potential for an SFA with graphene surfaces doped in varying ways.[70] By exploring these and other situations the use of graphene can be optimized to create new technologies that are tunable, efficient, and resilient.

REFERENCES

1. Novoselov, K. S.; Geim, A. K.; Morozov, S. V.; Jiang, D.; Zhang, Y.; Dubonos, S. V.; Grigorieva, I. V.; Firsov, A. A., Electric field effect in atomically thin carbon films. *Science* **2004,** *306* (5696), 666-9.

2. Huang, X.; Yin, Z.; Wu, S.; Qi, X.; He, Q.; Zhang, Q.; Yan, Q.; Boey, F.; Zhang, H., Graphene-based materials: synthesis, characterization, properties, and applications. *Small* **2011,** *7* (14), 1876-902.

3. Du, X.; Skachko, I.; Barker, A.; Andrei, E. Y., Approaching ballistic transport in suspended graphene. *Nat Nanotechnol* **2008,** *3* (8), 491-5.

4. Lee, C.; Wei, X.; Kysar, J. W.; Hone, J., Measurement of the elastic properties and intrinsic strength of monolayer graphene. *Science* **2008,** *321* (5887), 385-8.

5. Kim, K. S.; Lee, H. J.; Lee, C.; Lee, S. K.; Jang, H.; Ahn, J. H.; Kim, J. H.; Lee, H. J., Chemical vapor deposition-grown graphene: the thinnest solid lubricant. *ACS Nano* **2011,** *5* (6), 5107-14.

6. Dienwiebel, M.; Verhoeven, G. S.; Pradeep, N.; Frenken, J. W. M.; Heimberg, J. A.; Zandbergen, H. W., Superlubricity of Graphite. *Physical Review Letters* **2004,** *92* (12), 126101.

7. Hone, J.; Carpick, R. W., Friction. Slippery when dry. *Science* **2015,** *348* (6239), 1087-8.

8. Ashraf, A.; Wu, Y.; Wang, M. C.; Aluru, N. R.; Dastgheib, S. A.; Nam, S., Spectroscopic investigation of the wettability of multilayer graphene using highly ordered pyrolytic graphite as a model material. *Langmuir* **2014,** *30* (43), 12827-36.

9. Li, Z.; Wang, Y.; Kozbial, A.; Shenoy, G.; Zhou, F.; McGinley, R.; Ireland, P.; Morganstein, B.; Kunkel, A.; Surwade, S. P.; Li, L.; Liu, H., Effect of airborne contaminants on the wettability of supported graphene and graphite. *Nat Mater* **2013,** *12* (10), 925-31.

10. Schrader, M. E., Ultrahigh vacuum techniques in the measurement of contact angles. IV. Water on graphite (0001). *The Journal of Physical Chemistry* **1975,** *79* (23), 2508-2515.

11. Berman, D.; Deshmukh, S. A.; Sankaranarayanan, S. K.; Erdemir, A.; Sumant, A. V., Friction. Macroscale superlubricity enabled by graphene nanoscroll formation. *Science* **2015,** *348* (6239), 1118-22.

12. Vilhena, J. G.; Pimentel, C.; Pedraz, P.; Luo, F.; Serena, P. A.; Pina, C. M.; Gnecco, E.; Perez, R., Atomic-Scale Sliding Friction on Graphene in Water. *ACS Nano* **2016,** *10* (4), 4288-93.

13. Robinson, B. J.; Kay, N. D.; Kolosov, O. V., Nanoscale interfacial interactions of graphene with polar and nonpolar liquids. *Langmuir* **2013,** *29* (25), 7735-42.

14. Ye, Z.; Egberts, P.; Han, G. H.; Johnson, A. T.; Carpick, R. W.; Martini, A., Load-Dependent Friction Hysteresis on Graphene. *ACS Nano* **2016,** *10* (5), 5161-8.

15. Lee, H.; Ko, J. H.; Choi, J. S.; Hwang, J. H.; Kim, Y. H.; Salmeron, M.; Park, J. Y., Enhancement of Friction by Water Intercalated between Graphene and Mica. *J Phys Chem Lett* **2017,** *8* (15), 3482-3487.

16. Thompson, P. A.; Robbins, M. O.; Grest, G. S., Structure and Shear Response in Nanometer-Thick Films. *Isr J Chem* **1995,** *35* (1), 93-106.

17. Urbakh, M.; Klafter, J.; Gourdon, D.; Israelachvili, J., The nonlinear nature of friction. *Nature* **2004,** *430* (6999), 525-8.

18. Ortiz-Young, D.; Chiu, H. C.; Kim, S.; Voitchovsky, K.; Riedo, E., The interplay between apparent viscosity and wettability in nanoconfined water. *Nat Commun* **2013,** *4*, 2482.

19. Savage, R. H., Graphite Lubrication. *J Appl Phys* **1948,** *19* (1), 1-10.

20. Levita, G.; Restuccia, P.; Righi, M. C., Graphene and MoS2 interacting with water: A comparison by ab initio calculations. *Carbon* **2016,** *107*, 878-884.

21. Cohen-Tanugi, D.; Grossman, J. C., Water desalination across nanoporous graphene. *Nano Lett* **2012,** *12* (7), 3602-8.

22. Radha, B.; Esfandiar, A.; Wang, F. C.; Rooney, A. P.; Gopinadhan, K.; Keerthi, A.; Mishchenko, A.; Janardanan, A.; Blake, P.; Fumagalli, L.; Lozada-Hidalgo, M.; Garaj, S.; Haigh, S. J.; Grigorieva, I. V.; Wu, H. A.; Geim, A. K., Molecular transport through capillaries made with atomic-scale precision. *Nature* **2016,** *538* (7624), 222-225.

23. Majumder, M.; Chopra, N.; Andrews, R.; Hinds, B. J., Nanoscale hydrodynamics: enhanced flow in carbon nanotubes. *Nature* **2005,** *438* (7064), 44.

24. Huang, D. M.; Sendner, C.; Horinek, D.; Netz, R. R.; Bocquet, L., Water slippage versus contact angle: a quasiuniversal relationship. *Phys Rev Lett* **2008,** *101* (22), 226101.

25. Xie, Q.; Alibakhshi, M. A.; Jiao, S.; Xu, Z.; Hempel, M.; Kong, J.; Park, H. G.; Duan, C., Fast water transport in graphene nanofluidic channels. *Nat Nanotechnol* **2018,** *13* (3), 238-245.

26. Celebi, A. T.; Barisik, M.; Beskok, A., Surface charge-dependent transport of water in graphene nano-channels. *Microfluidics and Nanofluidics* **2017,** *22* (1), 7.

27. Kannam, S. K.; Todd, B. D.; Hansen, J. S.; Daivis, P. J., Slip length of water on graphene: Limitations of non-equilibrium molecular dynamics simulations. *The Journal of Chemical Physics* **2012,** *136* (2), 024705.

28. Wang, M. C.; Chun, S.; Han, R. S.; Ashraf, A.; Kang, P.; Nam, S., Heterogeneous, three-dimensional texturing of graphene. *Nano Lett* **2015,** *15* (3), 1829-35.

29. Lee, C.; Li, Q.; Kalb, W.; Liu, X. Z.; Berger, H.; Carpick, R. W.; Hone, J., Frictional characteristics of atomically thin sheets. *Science* **2010,** *328* (5974), 76-80.

30. Spikes, H., Stress-augmented thermal activation: Tribology feels the force. *Friction* **2018,** *6* (1), 1-31.

31. Eyring, H., The activated complex in chemical reactions. *Journal of Chemical Physics* **1935,** *3* (2), 107-115.

32. Eyring, H., Viscosity, plasticity, and diffusion as examples of absolute reaction rates. *Journal of Chemical Physics* **1936,** *4* (4), 283-291.

33. Lichter, S.; Martini, A.; Snurr, R. Q.; Wang, Q., Liquid slip in nanoscale channels as a rate process. *Phys Rev Lett* **2007,** *98* (22), 226001.

34. Hutter, J. L.; Bechhoefer, J., Calibration of atomic-force microscope tips. *Review of Scientific Instruments* **1993,** *64* (7), 1868-1873.

35. Mullin, N.; Hobbs, J. K., A non-contact, thermal noise based method for the calibration of lateral deflection sensitivity in atomic force microscopy. *Rev Sci Instrum* **2014,** *85* (11), 113703.

36. Li, Q. Y.; Lee, C.; Carpick, R. W.; Hone, J., Substrate effect on thickness-dependent friction on graphene. *Phys Status Solidi B* **2010,** *247* (11-12), 2909-2914.

37. Israelachvili, J. N., *Intermolecular and Surface Forces*. Elsevier Science: 2011.

38. Iler, R. K., The chemistry of silica. Wiley, New York: 1979.

39. Yin, J.; Zhang, Z.; Li, X.; Yu, J.; Zhou, J.; Chen, Y.; Guo, W., Waving potential in graphene. *Nat Commun* **2014,** *5*, 3582.

40. Zachariah, Z.; Espinosa-Marzal, R. M.; Heuberger, M. P., Ion specific hydration in nano-confined electrical double layers. *J Colloid Interface Sci* **2017,** *506* (Supplement C), 263-270.

41. Schlegel, M. L.; Nagy, K. L.; Fenter, P.; Cheng, L.; Sturchio, N. C.; Jacobsen, S. D., Cation sorption on the muscovite (001) surface in chloride solutions using high-resolution X-ray reflectivity. *Geochimica et Cosmochimica Acta* **2006,** *70* (14), 3549-3565.

42. Pashley, R. M., Dlvo and Hydration Forces between Mica Surfaces in Li+,Na+,K+,and Cs+ Electrolyte-Solutions - a Correlation of Double-Layer and Hydration Forces with Surface Cation-Exchange Properties. *J Colloid Interf Sci* **1981,** *83* (2), 531-546.

43. Williams, C. D.; Dix, J.; Troisi, A.; Carbone, P., Effective Polarization in Pairwise Potentials at the Graphene-Electrolyte Interface. *J Phys Chem Lett* **2017,** *8* (3), 703-708.

44. Heller, I.; Chatoor, S.; Mannik, J.; Zevenbergen, M. A.; Dekker, C.; Lemay, S. G., Influence of electrolyte composition on liquid-gated carbon nanotube and graphene transistors. *J Am Chem Soc* **2010,** *132* (48), 17149-56.

45. Chen, F.; Qing, Q.; Xia, J.; Li, J.; Tao, N., Electrochemical gate-controlled charge transport in graphene in ionic liquid and aqueous solution. *J Am Chem Soc* **2009,** *131* (29), 9908-9.

46. Shi, G.; Ding, Y.; Fang, H., Unexpectedly strong anion-pi interactions on the graphene flakes. *J Comput Chem* **2012,** *33* (14), 1328-37.

47. Emami, F. S.; Puddu, V.; Berry, R. J.; Varshney, V.; Patwardhan, S. V.; Perry, C. C.; Heinz, H., Force Field and a Surface Model Database for Silica to Simulate Interfacial Properties in Atomic Resolution. *Chem Mater* **2014,** *26* (8), 2647-2658.

48. Sharma, P.; Miskovic, Z. L., Ionic screening of charged impurities in electrolytically gated graphene: A partially linearized Poisson-Boltzmann model. *J Chem Phys* **2015,** *143* (13), 134118.

49. Chen, F.; Xia, J.; Tao, N., Ionic screening of charged-impurity scattering in graphene. *Nano Lett* **2009,** *9* (4), 1621-5.

50. Israelachvili, J. N.; Pashley, R. M., Molecular Layering of Water at Surfaces and Origin of Repulsive Hydration Forces. *Nature* **1983,** *306* (5940), 249-250.

51. Kilpatrick, J. I.; Loh, S. H.; Jarvis, S. P., Directly probing the effects of ions on hydration forces at interfaces. *J Am Chem Soc* **2013,** *135* (7), 2628-34.

52. Espinosa-Marzal, R. M.; Drobek, T.; Balmer, T.; Heuberger, M. P., Hydrated-ion ordering in electrical double layers. *Phys Chem Chem Phys* **2012,** *14* (17), 6085-93.

53. Smith, D. W., Ionic hydration enthalpies. *Journal of Chemical Education* **1977,** *54* (9), 540.

54. Jiang, G. P.; Cheng, C.; Li, D.; Liu, J. Z., Molecular dynamics simulations of the electric double layer capacitance of graphene electrodes in mono-valent aqueous electrolytes. *Nano Res* **2016,** *9* (1), 174-186.

55. Kjellander, R.; Marcelja, S., Correlation and Image Charge Effects in Electric Double-Layers. *Chem Phys Lett* **1984,** *112* (1), 49-53.

56. Peng, Y.; Wang, Z.; Zou, K., Friction and Wear Properties of Different Types of Graphene Nanosheets as Effective Solid Lubricants. *Langmuir* **2015,** *31* (28), 7782-91.

57. Spikes, H.; Tysoe, W., On the Commonality Between Theoretical Models for Fluid and Solid Friction, Wear and Tribochemistry. *Tribology Letters* **2015,** *59* (1), 21.

58. Ma, L.; Gaisinskaya-Kipnis, A.; Kampf, N.; Klein, J., Origins of hydration lubrication. *Nat Commun* **2015,** *6*, 6060.

59. Briscoe, B.; Evans, D. In *The shear properties of Langmuir-Blodgett layers*, The Royal Society: 1982; pp 389-407.

60. Raghuraman, S.; Elinski, M. B.; Batteas, J. D.; Felts, J. R., Driving Surface Chemistry at the Nanometer Scale Using Localized Heat and Stress. *Nano Letters* **2017,** *17* (4), 2111-2117.

61. Chowdhuri, S.; Chandra, A., Molecular dynamics simulations of aqueous NaCl and KCl solutions: Effects of ion concentration on the single-particle, pair, and collective dynamical properties of ions and water molecules. *The Journal of Chemical Physics* **2001,** *115* (8), 3732-3741.

62. Bonaccurso, E.; Kappl, M.; Butt, H.-J., Hydrodynamic Force Measurements: Boundary Slip of Water on Hydrophilic Surfaces and Electrokinetic Effects. *Physical Review Letters* **2002,** *88* (7), 076103.

63. Cafolla, C.; Voitchovsky, K., Lubricating properties of single metal ions at interfaces. *Nanoscale* **2018,** *10* (25), 11831-11840.

64. Choi, W.; Ulissi, Z. W.; Shimizu, S. F.; Bellisario, D. O.; Ellison, M. D.; Strano, M. S., Diameter-dependent ion transport through the interior of isolated single-walled carbon nanotubes. *Nat Commun* **2013,** *4*, 2397.

65. Abraham, J.; Vasu, K. S.; Williams, C. D.; Gopinadhan, K.; Su, Y.; Cherian, C. T.; Dix, J.; Prestat, E.; Haigh, S. J.; Grigorieva, I. V.; Carbone, P.; Geim, A. K.; Nair, R. R., Tunable sieving of ions using graphene oxide membranes. *Nat. Nanotechnol.* **2017,** *12* (6), 546-+.

66. Huttmann, F.; Martinez-Galera, A. J.; Caciuc, V.; Atodiresei, N.; Schumacher, S.; Standop, S.; Hamada, I.; Wehling, T. O.; Blugel, S.; Michely, T., Tuning the van der Waals Interaction of Graphene with Molecules via Doping. *Physical Review Letters* **2015,** *115* (23), 236101.

67. Schumacher, S.; Wehling, T. O.; Lazic, P.; Runte, S.; Forster, D. F.; Busse, C.; Petrovic, M.; Kralj, M.; Blugel, S.; Atodiresei, N.; Caciuc, V.; Michely, T., The backside of graphene: manipulating adsorption by intercalation. *Nano Letters* **2013,** *13* (11), 5013-9.

68. Anand, A.; Unnikrishnan, B.; Mao, J.-Y.; Lin, H.-J.; Huang, C.-C., Graphene-based nanofiltration membranes for improving salt rejection, water flux and antifouling–A review. *Desalination* **2018,** *429*, 119-133.

69. Ashraf, A.; Wu, Y.; Wang, M. C.; Yong, K.; Sun, T.; Jing, Y.; Haasch, R. T.; Aluru, N. R.; Nam, S., Doping-Induced Tunable Wettability and Adhesion of Graphene. *Nano Lett* **2016,** *16* (7), 4708-12.

70. Britton, J.; Cousens, N. E.; Coles, S. W.; van Engers, C. D.; Babenko, V.; Murdock, A. T.; Koos, A.; Perkin, S.; Grobert, N., A graphene surface force balance. *Langmuir* **2014,** *30* (38), 11485-92.

71. Tsoi, S.; Dev, P.; Friedman, A. L.; Stine, R.; Robinson, J. T.; Reinecke, T. L.; Sheehan, P. E., van der Waals Screening by Single-Layer Graphene and Molybdenum Disulfide. *Acs Nano* **2014,** *8* (12), 12410-12417.

72. Lai, C. Y.; Tang, T. C.; Amadei, C. A.; Marsden, A. J.; Verdaguer, A.; Wilson, N.; Chiesa, M., A nanoscopic approach to studying evolution in graphene wettability. *Carbon* **2014,** *80*, 784-792.

73. Lipkin, D. M.; Israelachvili, J. N.; Clarke, D. R., Estimating the metal-ceramic van der Waals adhesion energy. *Philosophical Magazine A* **1997,** *76* (4), 715-728.

74. Kocherlakota, L. S.; Krajina, B. A.; Overney, R. M., Communication: Local energetic analysis of the interfacial and surface energies of graphene from the single layer to graphite. *The Journal of Chemical Physics* **2015,** *143* (24), 241105.

75. Jurado, L. A.; Espinosa-Marzal, R. M., Insight into the Electrical Double Layer of an Ionic Liquid on Graphene. *Sci Rep* **2017,** *7* (1), 4225.

76. Tivony, R.; Klein, J., Probing the Surface Properties of Gold at Low Electrolyte Concentration. *Langmuir* **2016,** *32* (29), 7346-7355.

77. Chhabra, R. P., Non-Newtonian fluids: An introduction. Springer: 2010.

78. Dickinson, J. T.; Park, N. S.; Kim, M. W.; Langford, S. C., A scanning force microscope study of a tribochemicalsystem: stress-enhanced dissolution. *Tribology Letters* **1997,** *3* (1), 69-80.

APPENDIX A: DLVO MODEL

The following expression gives the DLVO force for dissimilar surfaces as the sum of van der Waals (F_{VDW}) and electric double layer forces (F_{EDL}):

$$\frac{F_{DLVO}}{R_{eff}} = \frac{F_{VDW}}{R_{eff}} + \frac{F_{EDL}}{R_{eff}} = -\frac{A_H}{6D^2} + 2\pi\varepsilon\varepsilon_0\kappa\frac{(2\phi_T\phi_G - (\phi_T^2+\phi_G^2)\exp(-\kappa D))}{\exp(\kappa D)-\exp(-\kappa D)} \quad \text{Eq. (3)}$$

A_H being the Hamaker constant, D the separation between tip and graphene, $R_{eff} = R$ the radius of the tip (R=50 nm in normal force measurements), κ the inverse of the Debye length, ϕ_G the electrochemical potential at the Outer Helmholtz plane above graphene (OHP potential of graphene), ϕ_T the OHP potential of the AFM tip, ε the relative permittivity of the solution (unitless) and ε_0 the vacuum permittivity.

The expression for van der Waals forces (F_{VDW}) assumes no transparency of graphene to dispersion interactions between the tip and the underlying substrate.[71-72] The Lipkin theory[73] was used to estimate the Hamaker constant of graphene and tip (considered to be naturally oxidized silicon, i.e. SiO_2) in air with refractive index n_{SiO_2}=1.47 and vibration frequency ν_{e,SiO_2}=3.2·10^{15} s^{-1}, and for graphene, $\nu_{e,G}$ =4·10^{15} s^{-1}, which yields $A_{H,air}$ ~1.52·10^{-19} J, close to reported experimental and theoretical values for HOPG (1.35·10^{-19} J in ref.[74]). According to the mixing rule,[37] the Hamaker constant is reduced to ~2.73·10^{-20} J in water, calculated with following values for the refractive index of water n_w=1.337 and the relative permittivity of water and silicon dioxide, ϵ_w=78 and ϵ_{SiO_2}=3.8, respectively.

The expression for the EDL force (F_{EDL}, second term in Eq. 3) assumes constant surface potential for both the tip and the graphene surface. Fits of the experimental data to the DLVO equation were also carried out under the assumption of constant surface charge for the graphene and constant

surface potential for the tip,[75] and the results are qualitatively similar. It is important to emphasize, that the expression for the EDL force was derived from a linearization of the Poisson-Boltzman equation that is only strictly valid for small potentials (<25 mV). The errors introduced by this linearized approach are typically not excessive for potentials as high as 200 mV, except for distances that are significantly shorter than one Debye length. The maximum OHP potential of graphene in the selected electrolyte solutions is ~-60 mV, and hence, the estimated values should be considered a good approximation, except at the concentration of 100 mM, where higher errors are possible due to the collapse of the EDL. Further, the model neglects that a charge regulation can happen at the closest separations, as observed for metals;[76] more studies are needed to clarify this phenomenon. Note that the OHP is located at a small distance away from the surface, between the Stern and the diffuse layers. The surface potential or charge directly at the graphene plane cannot be obtained from the fits of the experimental results to Eq. 3, because the EDL theory assumes that ions are strongly bound to the surface and are immobile in the Stern layer, and Eq. 3 only applies to the mobile ions in the diffuse layer. The absolute zero in the force measurements is not known with high precision, and hence, the obtained fitting parameters need to be considered with caution.

APPENDIX B: ADDITIONAL MEASUREMENTS

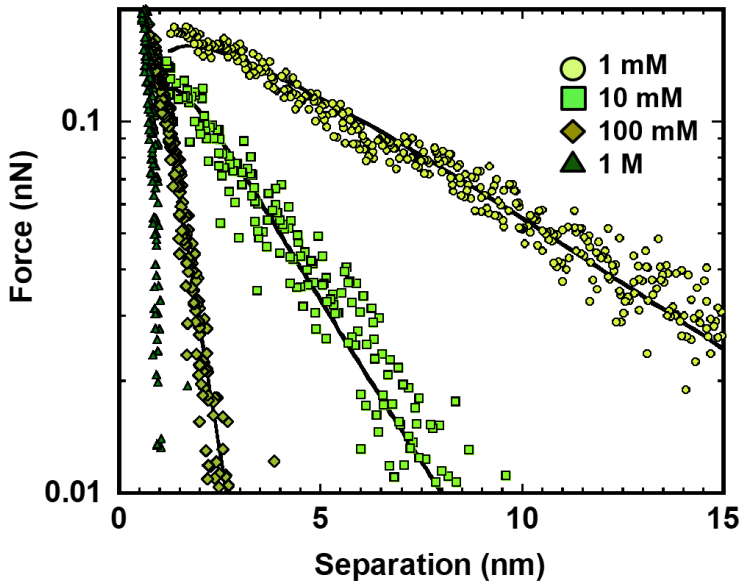

Figure 6. Surface force between graphene and the (naturally oxidized) silicon AFM tip in KCl solutions at the concentrations of 1 mM (circles, yellow green), 10 mM (squares, light green), 100 mM (diamonds, green) and 1M (triangles, dark green). The OHP potential of the tip (R=50 nm) obtained from the fits in water and KCl is: -123 mV (water), -130 mV (1 mM), -88 mV (10 mM), -33 mV (100 mM).

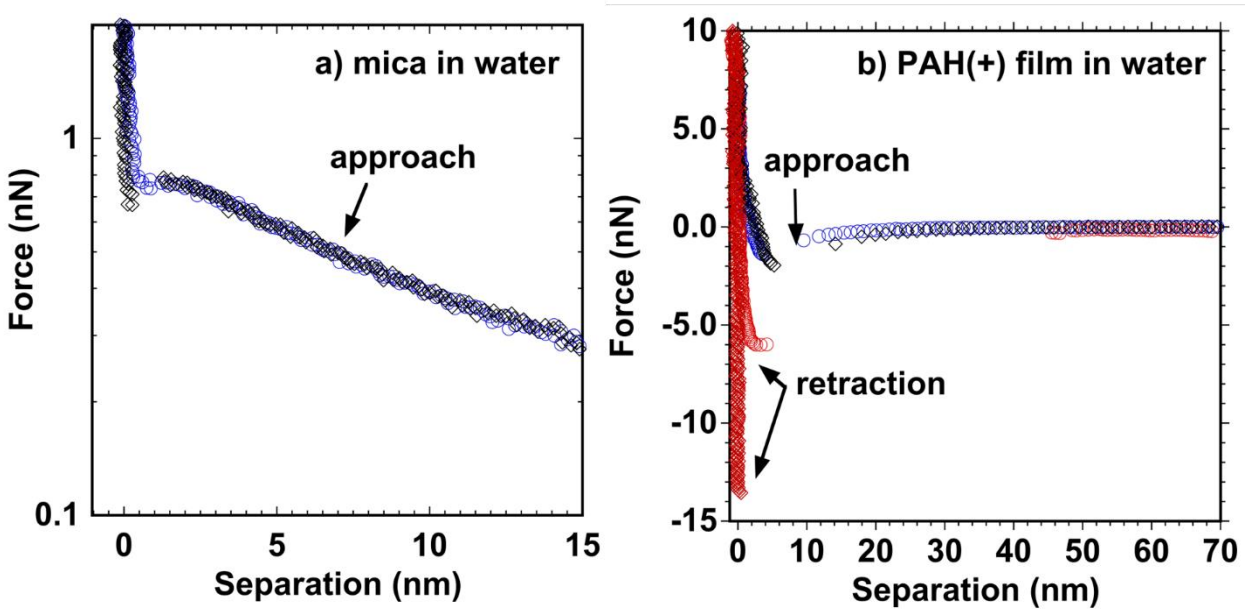

Figure 7. Representative surface force between a silicon AFM tip and (a) mica and (b) a poly allylamine hydrochloride (PAH, M_W=17500 g/mol) film as a function of separation in water. The attraction of the tip to the positively charged PAH film and repulsion from the (negatively charged) mica unambiguously demonstrate that the tip surface (silicon dioxide) is negatively charged in the aqueous solutions. Mica was cleaved immediately before the experiments to limit exposure to ambient air. Adsorption of PAH was performed by immersing the freshly cleaved mica in a solution of 1 mg/mL PAH and 500 mM NaCl for 45 min. The PAH-coated mica was then thoroughly rinsed with ultrapure water and again equilibrated in ultrapure water before the force measurement.

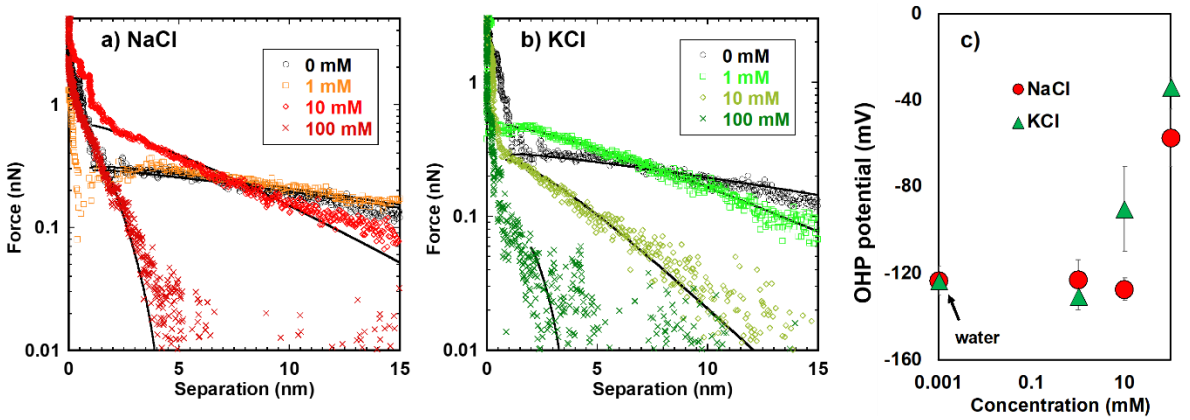

Figure 8. Representative surface forces between a naturally oxidized silicon wafer (Si/SiO_2 substrate) and a (naturally oxidized) silicon AFM tip in (a) NaCl (red shades) and (b) KCl (green shades) solutions and in water (black). (c) OHP potential of silicon oxide in the selected electrolyte solutions determined by fitting the force *vs.* distance data to the DLVO theory, Eq. 3 (black lines in a and b) under the assumption of chemically similar surfaces (silicon dioxide) and constant surface potential. The OHP potential of silicon dioxide is negative under all conditions, but its magnitude becomes less negative with increase in concentration of the two electrolytes. This indicates that the ions (Na^+ and K^+) within the Stern layer compensate the surface charge more effectively with an increase in concentration. Tip radius=50 nm.

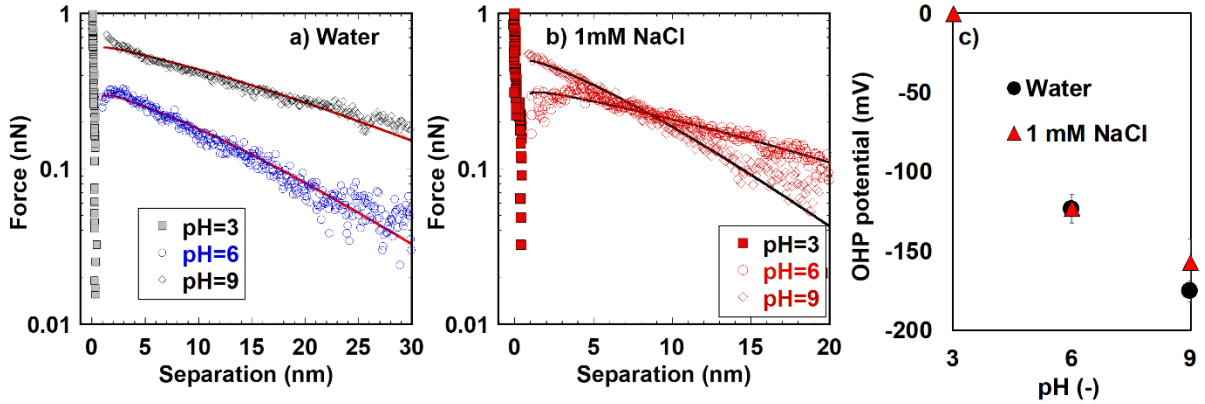

Figure 9. Representative surface forces between a (naturally oxidized) silicon wafer (Si/SiO_2 substrate) and a (naturally oxidized) silicon AFM tip (Radius=50 nm) in (a) water and (b) 1mM NaCl solution at pH values of 3, 6, and 9. The electrical double layer at pH 3 is not detectable in either solution. (c) OHP potential of silicon oxide in the selected solutions as a function of pH. The OHP potential was determined by fitting the force *vs.* distance data to the DLVO theory, Eq. 3 (lines in a and b) under the assumption of chemically similar surfaces and constant surface potential. The OHP potential of silicon oxide is negative under all conditions, but its magnitude decreases with increasing pH, which is concurrent with the expected decrease in the concentration of hydronium ions in the Stern layer.

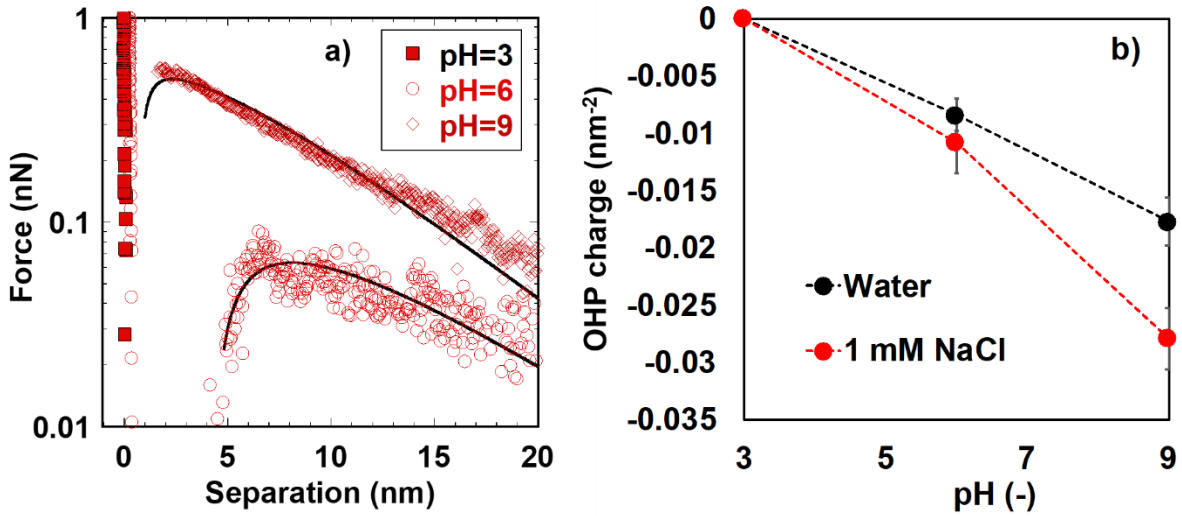

Figure 10. (a) Representative surface forces between graphene on Si/SiO_2 and a (naturally oxidized) silicon AFM tip (Radius=50 nm) in NaCl solution (1mM) at pH 3, 6, and 9. The electrical double layer at pH 3 is not detectable. (b) OHP charge of graphene in water and in 1mM NaCl at solution pH 3, 6, and 9, which was estimated by using the Debye Hückel approximation and the OHP potential determined by fitting the force *vs.* distance data to the DLVO equation, Eq. 3 (solid lines in a). Error bars give the standard deviation for 7-10 measurements.

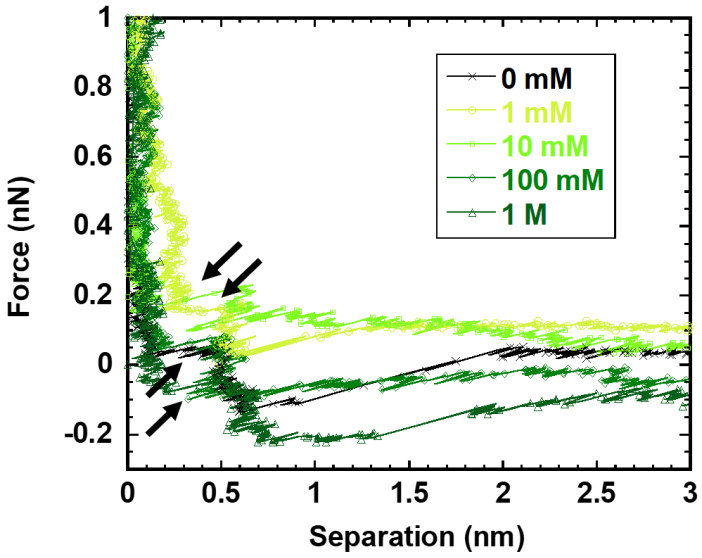

Figure 11. Surface forces between a (naturally oxidized) silicon AFM tip (radius=50 nm) and graphene in water and in KCl solutions at separations smaller than 3 nm. The arbitrary zero is selected at the hard wall measured at a force of 5 nN. Water is represented by the black markers, while green shades from light to dark represents increasing concentration (see legend). The arrows point at some of the resolved steps.

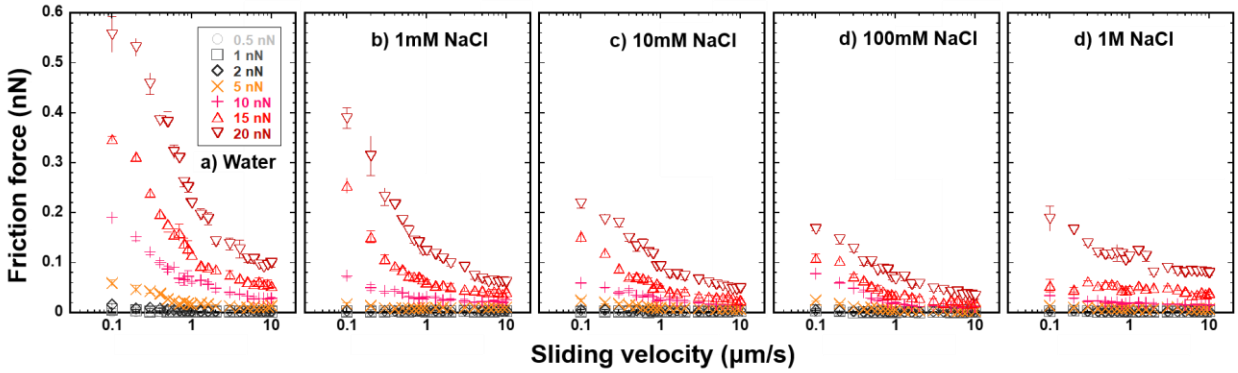

Figure 12. Friction force between the Si/SiO_2 substrate and a (naturally oxidized) silicon AFM tip as a function of sliding velocity at applied normal loads $\leq$ 20 nN in (a) water and (b-e) in NaCl solutions at different concentations. Error bars show variation of friction across 8 friction loops at the same conditions.

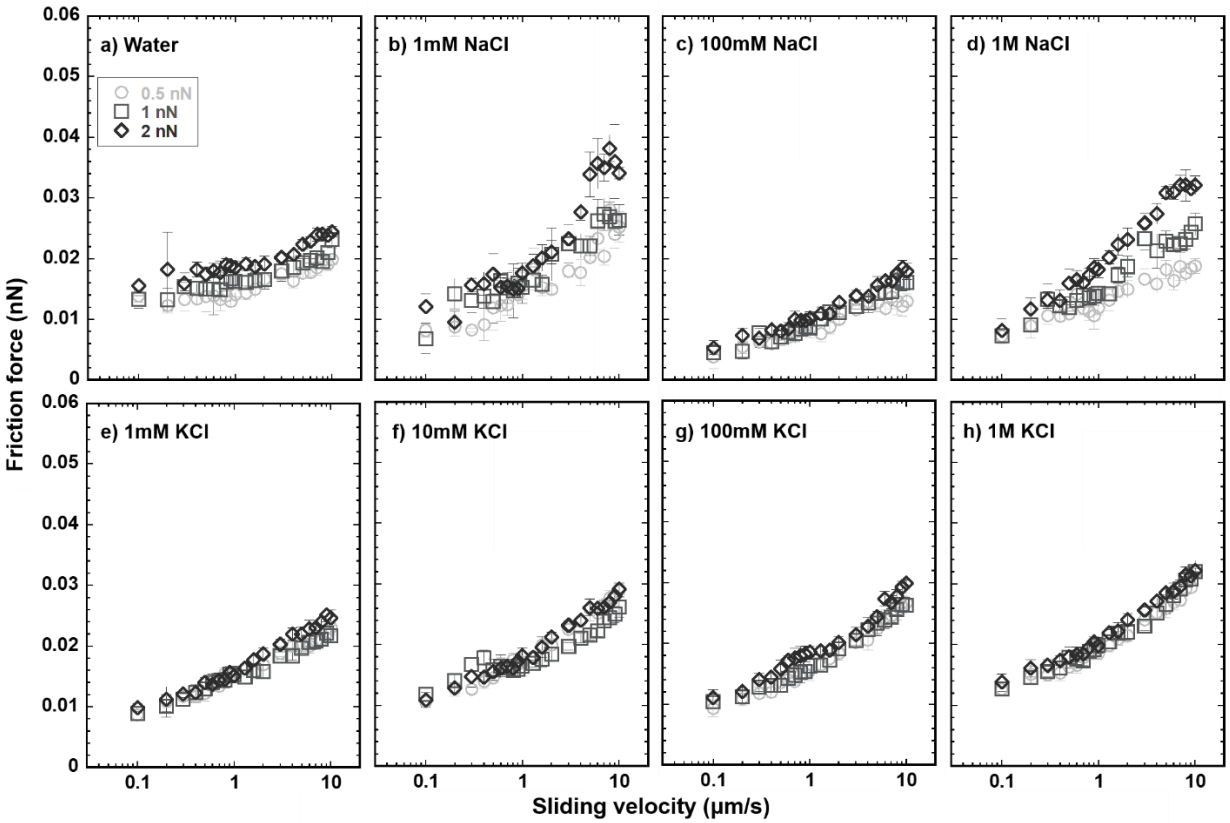

Figure 13. Friction force between graphene on Si/SiO_2 and a (naturally oxidized) silicon AFM tip as a function of sliding velocity at applied normal loads of 0.5, 1 and 2 nN in (a) water, (b-d) NaCl and (e-h) KCl solutions. Error bars show variation across eight friction loops. While fits in NaCl can still be obtained using a logarithmic function of the sliding velocity (Eq. 1-2), the R^2-values are better using a power law $\sim V^n$. Conversely, the fit of Eq. 2 to the measured friction force in

Figure 13 (cont.). KCl solutions within the same range of applied loads is reasonable ($0.95<R^2<0.99$). The power-dependence of friction on velocity is often interpreted as a viscous dissipation caused by the Couette flow of the confined liquid, as described by the Ostwald-de Waele equation[77] given by $F_L \sim A\eta_0(V/(D+b))^n$, A being the contact area, η_0 a constant, V/D the shear rate, n an exponent that can take any value and b the slip length. According to the discussion in the main text, it is reasonable that more ions and water are present in the confined film at low loads (<2 nN), especially in the case of NaCl solutions, where more layers were resolved, and the sodium cation is more strongly hydrated compared to potassium (Figure 2, inset). In our experiments, D cannot be unambiguously determined, and hence, we cannot apply this model to determine the slip length. Therefore, the shear-force measurements in NaCl solutions at loads smaller than 2 nN were not further analyzed in this work.

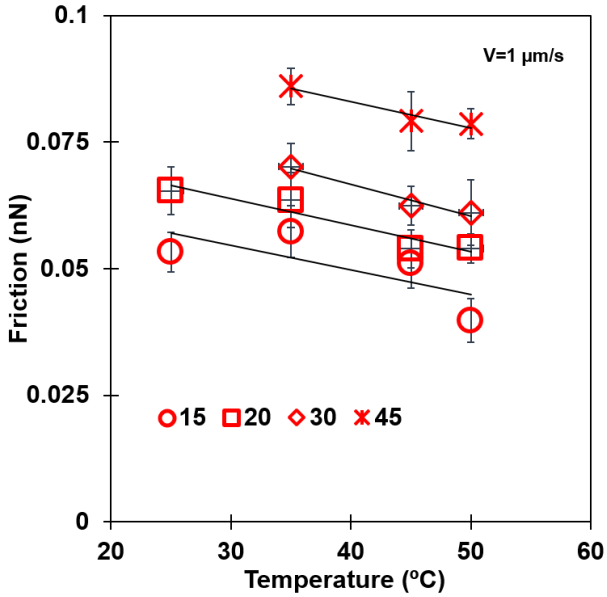

Figure 14. Friction force between graphene on Si/SiO_2 and an AFM tip as a function of the temperature at selected normal loads (15, 20, 30 and 45 nN) and at a constant sliding velocity of 1 μm/s.

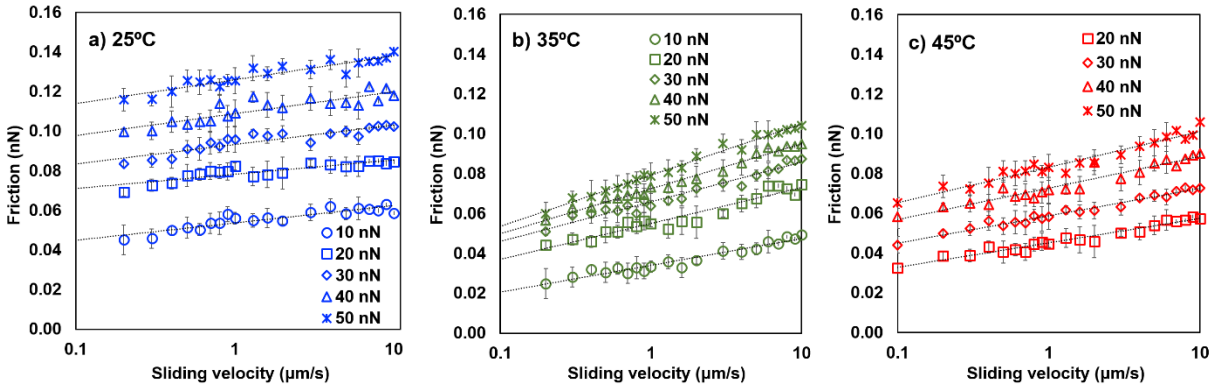

Figure 15. Friction force between graphene on Si/SiO_2 and an AFM tip as a function of sliding velocity in 1 mM NaCl at selected loads and temperatures: a) 25ºC, b) 35ºC and c) 45ºC. The error bars show the variation in friction across eight friction loops at each condition.

Reference Velocity

The narrow range of accessible temperatures in our AFM does not allow a precise determination of V_0, but we have performed two independent series of temperature-dependent measurements and have followed two different approaches to get more confidence on our results. First, the friction force was measured as a function of the normal load at various temperatures between 25 and 50ºC and at constant sliding velocity of 1 μm/s. Figure 14 shows that the friction force decreases linearly with the temperature in the selected range, i.e. $F_L \sim A' + B'T$. According to Eq. 2, the slope B' is given by $\frac{k_B}{\lambda}\ln\left(\frac{V}{V_0}\right)$. Averaging λ over the investigated range of temperatures enables one to determine V_0, which yields 48 m/s. Second, as shown in Figure 15, $F_L \sim A + B\ln(V)$, with $B = \frac{k_B T}{\lambda}$ and $A = \frac{E_a + L\gamma - k_B T \ln(V_0)}{\lambda}$ according to Eq. 2. The shear-activation length (λ) was determined for each load and temperature. The intercept of $A \cdot \lambda$ vs. load (L), yields $E_a - kT\ln(V_0)$. The slope of this parameter *vs.* temperature gives V_0. This approach yields V_0 =35 m/s. In the calculations for the data presented in the manuscript, we have assumed a value of V_0=40 m/s.

Reported values span from 20 m/s (for Langmuir Blodgett monolayers, estimated with a vibration frequency of 10^{11} s^{-1})[59] to 2500 m/s (for dissolved ions from calcite in an aqueous environment, estimated with a vibration frequency of 10^{13} s^{-1})[78], and therefore, our estimation is within the reported range.

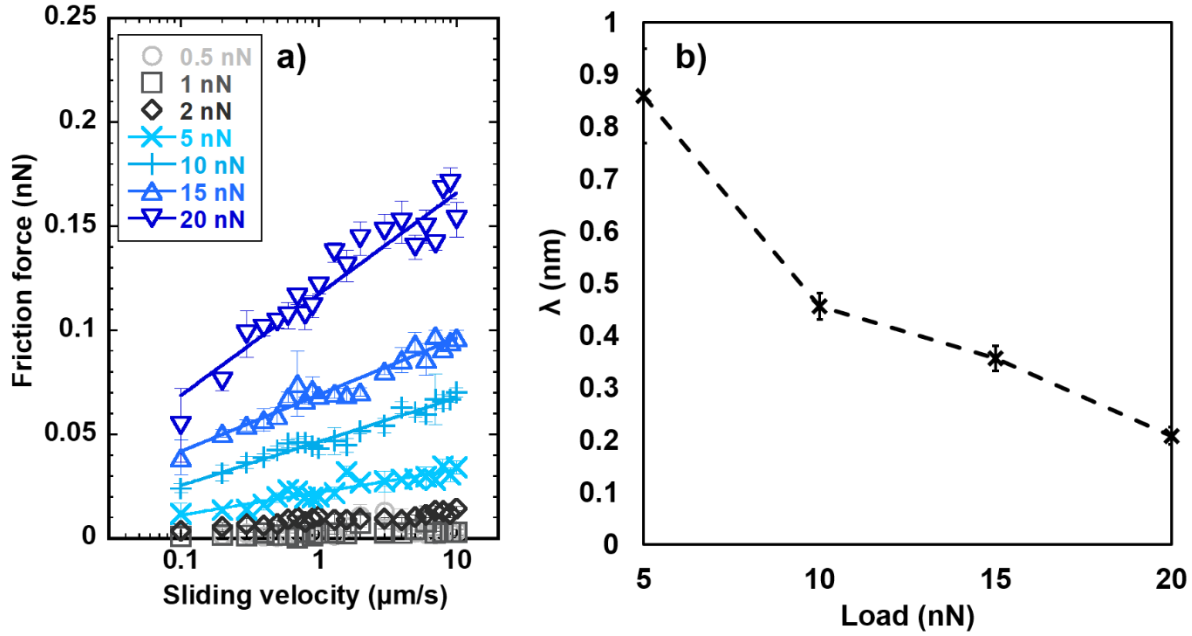

Figure 16. (a) Friction force between mica and an AFM tip as a function of velocity and normal load in water. The solid lines show the fits of Eq. 2 to the experimental results, which gives (b) the stress-activation length. The logarithmic fit for loads less than 5 nN was poor in water; results at these loads were better described by a power law fit, and therefore, the results were not further analyzed here (see Figure 13). Assuming the same reference velocity V_0 as for graphene (V_0=40 m/s) yields γ=0.0042±0.001 Å and E_a/k_BT=21.7±0.3. Error bars in (a) give the variation in friction across 8 friction loops, while in (b) they show the root mean square error from the fit of friction to Eq. 2. Radius of the tip is 34 nm.

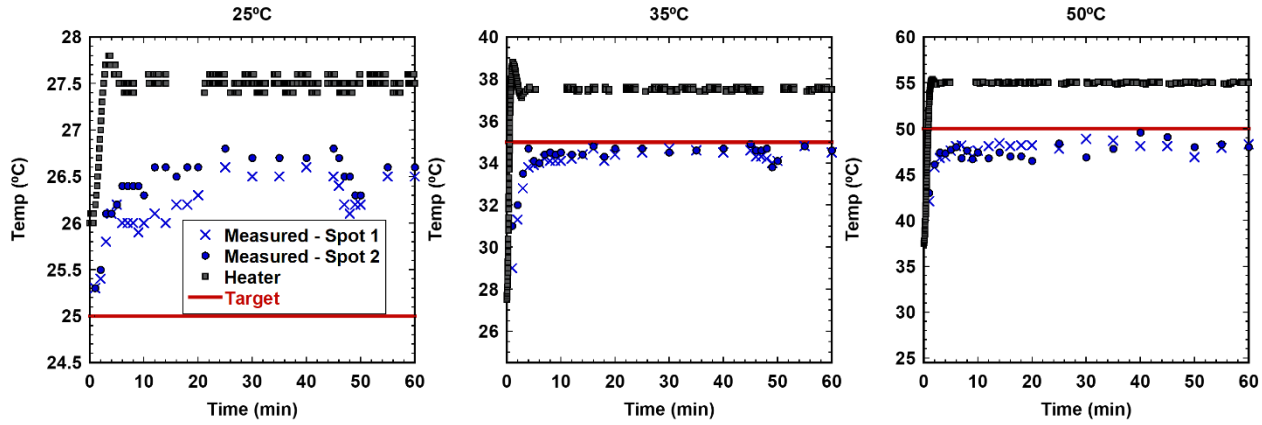

Figure 17. Representative temperature calibration measurements for the target solution temperatures of 25° C, 35° C, and 50° C (solid red lines). Black squares show the heater temperature measured by the JPK SPM software, while blue circles and crosses show the manually

Figure 17 (cont.) measured temperatures in the solution at two different locations in the petri dish. The 25° C measurements indicate that the heater should not be actively heating for room temperature experiments. The drops in measured temperature at ~45 minutes are due to increased measurement frequency during a 5 minutes period, which gave the system less time to equilibrate after each manual measurement of the temperature.